

Nonlinear Flow Past an Elliptic Mountain Ridge

HARALDUR ÓLAFSSON AND PHILIPPE BOUGEAULT

Météo-France, Centre National de Recherches Météorologiques, Toulouse, France

(Manuscript received 10 August 1995, in final form 12 February 1996)

ABSTRACT

The hydrostatic flow over an elliptical mountain of aspect ratio 5 is explored by numerical experiments. The upstream profiles of wind and stability are constant, the Coriolis effect is ignored, and there is free slip at the lower boundary. In these conditions, the flow characteristics depend mainly on the nondimensional mountain height, Nh/U . The authors have conducted experiments with Nh/U varying from 0.500 to 6.818. For low values of Nh/U , the results confirm the linear theory of Smith, which predicts stagnation aloft, leading to wave breaking and, on the upstream slope, leading to flow splitting. For higher values of Nh/U , the authors find that wave breaking ceases on the axis of symmetry but continues on each side of this axis. Even for the highest value of Nh/U used (6.818), significant areas of wave breaking and wave activity aloft are found. For all values of Nh/U , a substantial part of the flow is diverted vertically above the mountain. The detailed study of the kinematic pattern within the upstream blocking reveals an increasing tendency to small vortex creation when Nh/U increases. This, however, does not affect the main flow features. Finally, the authors observe the generation of potential vorticity in the wake of the mountain, leading to the creation of lee vortices. The potential vorticity pattern is very similar to the vorticity pattern shown by Schär and Smith for shallow-water flow. It is found to be insensitive to the turbulence parameterization in our model, as well as the general flow pattern. On the other hand, comparison with an experiment using a circular mountain reveals large differences in the elliptical case.

1. Introduction

Orographic effects on atmospheric flow have been investigated by numerous authors. A first approach concentrated on the generation and propagation of linear gravity waves (Queney 1948; Eliassen and Palm 1960), but during the last two decades, features like upstream deceleration, lee vortices, and wave breaking have gained attraction. Research on these features has partly been based on extensive field experiments, such as the ALPS Experiment (ALPEX) and the Pyrénées Experiment (PYREX), and observations around Hawaii. The present study was motivated by the PYREX program, which consisted of 10 short periods of intensive observations (IOPs) in 1990. The main objective of PYREX was to investigate the effects of a mountain range on the atmospheric momentum budget (Bougeault et al. 1993), but it has served for other related studies as well, such as local orographic winds (Georgelin and Richard 1996; Koffi 1994; Masson and Bougeault 1996), parameterization of surface friction (Georgelin et al. 1994), and investigation of lee waves (Satomura and Bougeault 1994).

Extensive literature exists on two-dimensional flow (e.g., Smith 1977; Stein 1992b) and three-dimensional flow around a circular mountain [e.g., Hunt and Snyder 1980; Smith 1980, 1989a,b; Smolarkiewicz and Rotunno (hereafter SR) 1989, 1990; Smith and Grønås 1993; Stein 1992a; Schär and Smith 1993a,b]. Comparatively little effort has been made to investigate in detail nonlinear flow around mountain ridges or mountains with high aspect ratio, although some results are shown by SR (1990). The lack of such a theoretical background for interpretation of the flow in PYREX has motivated the numerical simulations described in this paper.

Dimensional analysis (e.g., Smith and Grønås 1993) shows that the hydrostatic Boussinesq flow over an obstacle is governed by the obstacle shape, its aspect ratio, and its nondimensional height Nh/U , where N is the Brunt–Väisälä frequency, h is the obstacle (mountain) height, and U is the upstream wind; Nh/U can be regarded as the mountain height scaled by the vertical wavelength of a standing hydrostatic wave. Here, Nh is also the scale of the maximum horizontal velocity perturbations in a linear mountain wave, and Nh/U can therefore be regarded as a measure of nonlinearity; Nh/U is sometimes referred to as an inverse Froude number.

To investigate the three-dimensional flow over an idealized mountain ridge with aspect ratio 5, we have conducted a series of simulations with different values of Nh/U (see Table 1, line 1). The numbers in the name of each simulation refer to the value of Nh/U

Corresponding author address: Dr. Haraldur Ólafsson, CNRM/MC2, Météo-France, 42 Avenue G. Coriolis, F-31057 Toulouse, Cedex, France.
E-mail: olafsson@xdata.cnrm.meteo.fr

TABLE 1. A comparison of different parameters in our simulations. The singular points in lines 2 and 3 are nodes (N) and saddles (S). The potential vorticity (lines 13–15) is a mean value inside a square of 3×3 grid points. Line 19 shows the upstream height of the isentrope that acquires maximum steepening 1 cross-stream half-width away from the axis of symmetry.

Parameter	EX05	EX10	EX14	EX22	EX27	EX34	EX45	EX68	EX45NT	EX45c
1 Values of Nh/U	0.500	1.000	1.400	2.273	2.700	3.400	4.545	6.818	4.545	4.545
2 Singular points in the surface flow at $t^* = 16.2$ on the upstream side	0	0	1S + 1N	1S + 1N	1S + 1N	2S + 2N	2S + 2N	2S + 2N	2S + 2N	1S + 1N
3 Singular points in the surface flow at $t^* = 16.2$ on the lee side	0	0	2S + 2N	3S + 3N	3S + 3N	4S + 4N	3S + 3N	4S + 4N	4S + 4N	2S + 2N
4 h_s (m) (see Fig. 7)			1130	1850	2200	2770	3700	5520	4230	900
5 h_s/h (see Fig. 7)			0.81	0.81	0.82	0.82	0.81	0.81	0.93	0.20
6 Z_{0s} (m) (see Fig. 7)			170	1220	1470	2220	3350	5350	3320	920
7 Z_{0s}/h			0.12	0.54	0.54	0.65	0.74	0.79	0.73	0.20
8 $h - Z_{0s}$ (m)			1230	1053	1230	1180	1195	1468	1225	3625
9 $(h - Z_{0s})/h$			0.88	0.46	0.46	0.35	0.26	0.22	0.27	0.80
10 Maximum value of turbulence kinetic energy in the upstream blocking ($\text{m}^2 \text{s}^{-2}$)	0.0	0.0	0.4	0.9	1.6	2.0	2.6	3.6		0.8
11 Minimum value of u in the upstream blocking (m s^{-1})	0.63	0.06	-0.13	-0.17	-0.16	-0.33	-0.39	-0.42	-0.73	-0.08
12 Minimum value of u in the lee (m s^{-1})			-0.68	-1.24	-1.28	-1.48	-1.54	-1.67	-1.57	-1.12
13 PV at $z = 100$ m in the right vortex (facing downstream) (PV units)				2.5	3.0	3.5	4.0	4.1	4.0	
14 PV at $z = 0.1 h$ in the right vortex (facing downstream) (PV units)				2.0	2.0	2.0	2.5	2.8	2.3	
15 PV at $z = 0.1 h$ on the right shearline (facing downstream) (PV units)	0.2	0.5	1.9	1.6	1.9	2.1	1.8	2.4	2.4	1.3
16 Height of the lee vortices/ h			0.86	0.86	0.89	0.82	0.81	0.78	0.83	0.48
17 Maximum surface wind/ U	1.4	2.2	2.2	2.2	2.2	2.1	2.4	2.7	3.1	1.8
18 Maximum surface wind/ U on the axis of symmetry	1.4	2.2	2.2	2.0	1.9	2.0	1.8	1.7	1.9	1.1
19 Height of the maximum wave steepening on each side of the axis of symmetry/ h						0.80	0.82	0.83	0.82	

(EX14 has $Nh/U = 1.4$, etc.). One simulation, EX45NT (no turbulence), was conducted to investigate the effect of subgrid turbulence and EX45c (circular mountain) serves for validation purposes, as well as for comparison between flow past a circular mountain and a mountain ridge with aspect ratio 5.

2. The numerical calculations

a. The model

In this study, we use the former operational limited-area model of Météo-France, called PERIDOT (Imbard et al. 1986; Bougeault et al. 1991). PERIDOT is a primitive equation, hydrostatic model with a terrain-following vertical coordinate $\sigma = P/P_s$. The horizontal discretization is on the Arakawa C grid, and the time discretization uses the leapfrog method and a weak Asselin filter. The prognostic variables are the horizontal wind components, the temperature,

and the surface pressure. Humidity is also a prognostic variable but has been set to zero in our simulations. Together with steep isentropes, high concentration of turbulence kinetic energy is a major criterion for detection of wave breaking. Subgrid turbulence is computed by a “one-and-a-half” order closure scheme developed by Bougeault and Lacarrère (1989). In this scheme, the eddy coefficients are related to the turbulence kinetic energy through $K = C_k l_k \sqrt{e}$, where C_k is a constant, l_k is a vertical length scale, and e is the turbulence kinetic energy. For the evolution of the turbulence kinetic energy we have

$$\frac{\partial e}{\partial t} = -u \frac{\partial e}{\partial x} - v \frac{\partial e}{\partial y} - \dot{\sigma} \frac{\partial e}{\partial \sigma} - \frac{1}{\rho} \frac{\partial}{\partial z} \overline{\rho w' e'} - \overline{w' u'} \frac{\partial u}{\partial z} - \overline{w' v'} \frac{\partial v}{\partial z} + \beta \overline{w' \theta'} - \epsilon, \quad (1)$$

where u , v , w , and $\dot{\sigma}$ are motions in x , y , z , and σ directions, respectively, and θ is potential temperature.

TABLE 2. Values of different parameters upstream and downstream of the mountain in simulations with a circular mountain and $Nh/U = 4.545$; $u_{\min}^{\text{upstream}}$ is the maximum reverse wind speed in the upstream blocking, S and N are saddle and nodal points in the surface flow, and $u_{\min}^{\text{downstream}}$ is the maximum reverse wind speed between the lee vortices or their intensity; $S_1^{\text{downstream}}$ is the saddle between the vortices and the mountain, $S_2^{\text{downstream}}$ is the saddle downstream of the vortices and, Pos. ($u_{\min}^{\text{downstream}}$) is the distance from the mountain top to $u_{\min}^{\text{downstream}}$. "Dist. betw. vort." refers to the distance between the centers of the lee vortices, and the "Depth of vort." is the depth or the height of the lee vortices. SR refers to SR (1989) and SR (1990), and $t^* = U/L_y$ is a nondimensional time unit.

Parameter	SR ($t^* = 9.0$)	EX45c ($t^* = 8.1$)	EX45c ($t^* = 16.2$)
$u_{\min}^{\text{upstream}}$	$-0.02 U$	$-0.06 U$	$-0.08 U$
S^{upstream}	$-1.9 L$	$-2.3 L$	$-1.9 L$
N^{upstream}	$-1.1 L$	$-1.4 L$	$-1.4 L$
$u_{\min}^{\text{downstream}}$	$-1.45 U$	$-1.12 U$	$-0.73 U$
$S_1^{\text{downstream}}$	$0.4 L$	$0.7 L$	$0.7 L$
Pos. ($u_{\min}^{\text{downstream}}$)	$2.8 L$	$3.0 L$	$3.5 L$
Dist. betw. vort.	$2.2 L$	$2.1 L$	$2.1 L$
Width of wake	$4.3 L$	$3.6 L$	$3.8 L$
$S_2^{\text{downstream}}$	$4.5 L$	$5.0 L$	$6.3 L$
Depth of vort.	$0.65 h$	$0.57 h$	$0.48 h$

The terms in this equation are the horizontal and the vertical advection, the turbulent transport, the production by vertical wind shear, the buoyancy term, and the dissipation.

The turbulence scheme has been validated for convective situations and breaking waves (Bougeault and Lacarrere 1989) and for quasi-neutral flow (Masson and Bougeault 1996). The adiabatic part of PERIDOT has also been validated for two-dimensional as well as three-dimensional orographic flows by Stein (1992a,b).

b. Description of the simulations

The simulations were run in 40 vertical levels with a 10-km grid in a horizontal domain of 121×121 points except EX45c, which had a horizontal domain of 61×61 points. The mountain is described by

$$h(x, y) = \frac{h}{\left[1 + \left(\frac{x}{L_x}\right)^2 + \left(\frac{y}{L_y}\right)^2\right]^{1.5}}, \quad (2)$$

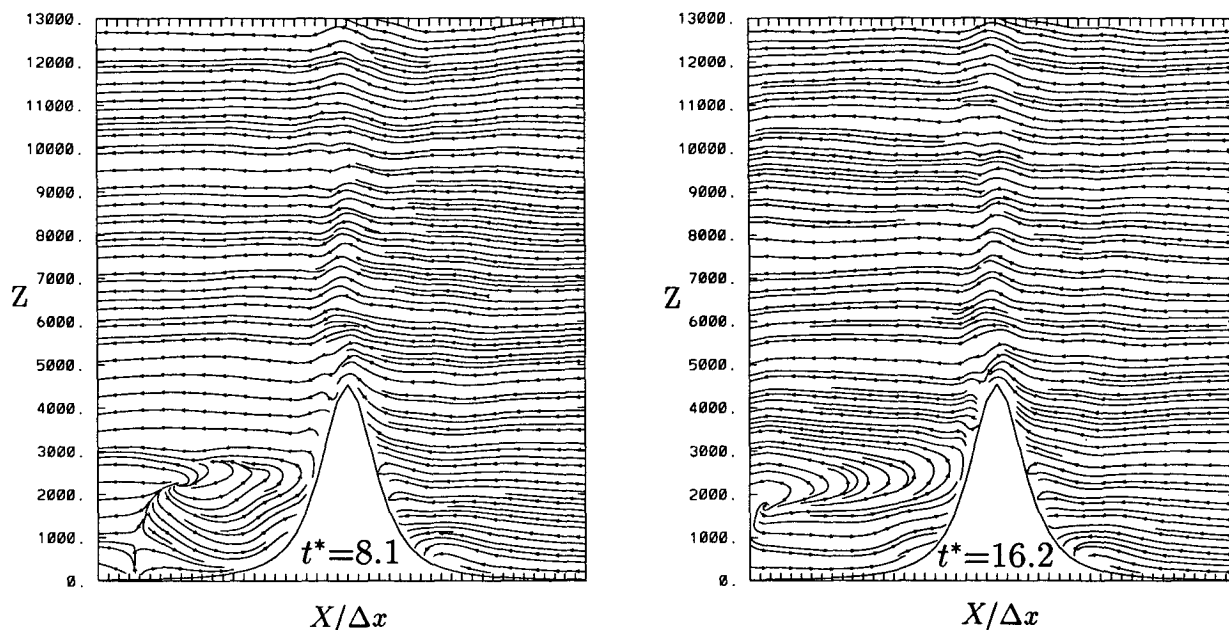


FIG. 1. Streamlines on the axis of symmetry in EX45c at 8.1 and 16.1 nondimensional time units. The flow is from right to left for comparison with SR [(1989), Fig. 3c].

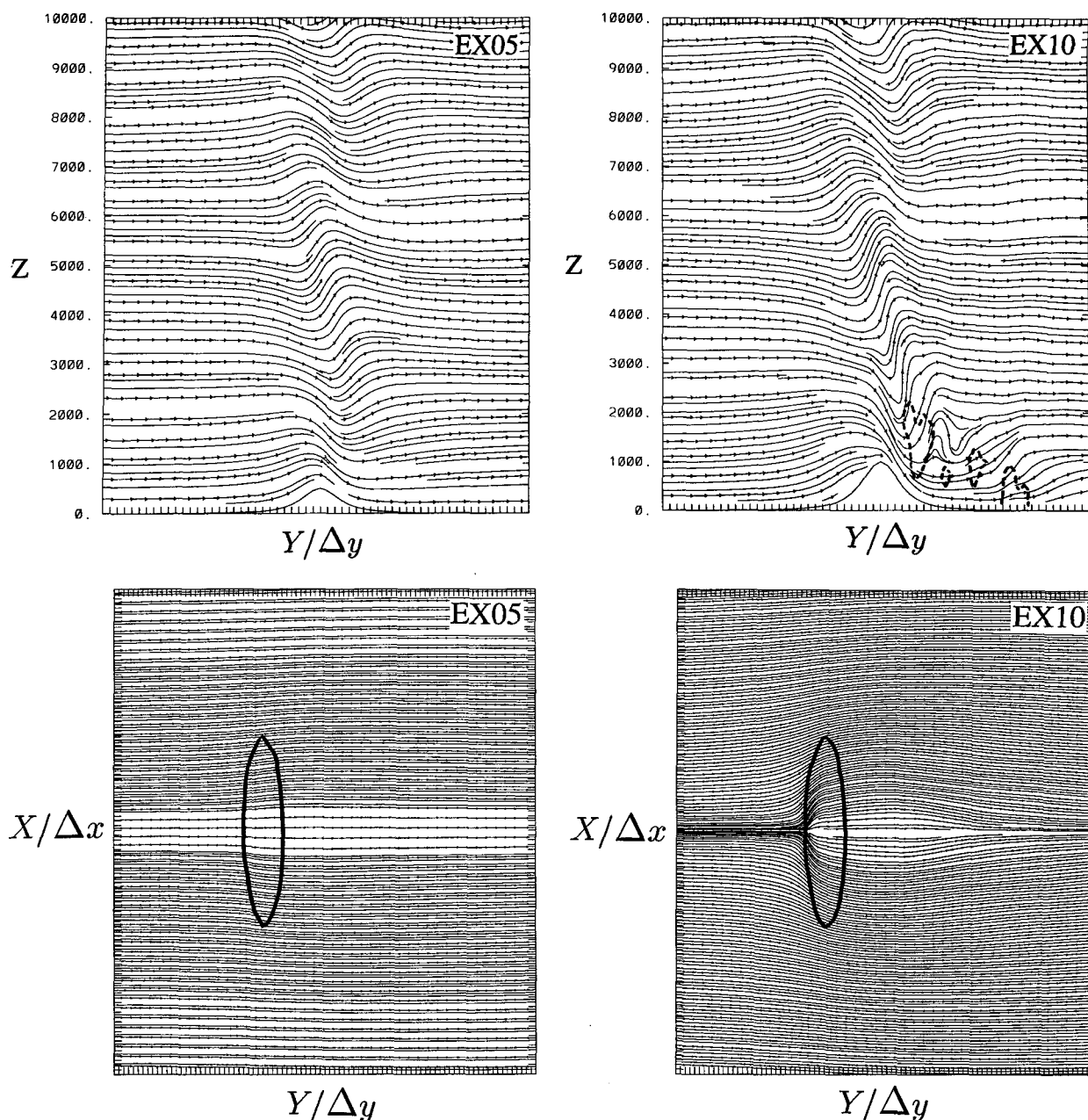


FIG. 2. Streamlines on the axis of symmetry and at the surface for different values of Nh/U and $R = 5$. The flow is from left to right. The horizontal plots show the topography at $0.35h$, and the vertical plots show the $0.5 \text{ m}^2 \text{ s}^{-2}$ isoline (dashed) of turbulence kinetic energy.

where h is the mountain-top height, and L_x and L_y are the mountain half-widths. This mountain shape has been used by Smith (1980, 1989b), Phillips (1984), SR (1990), and Stein (1992a) for different aspect ratios. Here, we set L_x to 200 km and L_y to 40 km, which is close to the values of the half-widths of the Pyrénées. This gives $R = L_x/L_y = 5$. EX45c has $L_x = L_y = 40 \text{ km}$.

The model is initialized everywhere with $U = 10 \text{ m s}^{-1}$ along the y axis and $N = 0.01 \text{ s}^{-1}$. The lateral boundary conditions are the same and constant in time. There is neither a large-scale pressure gradient nor a Coriolis force. Surface friction is set to zero everywhere. To prevent wave reflection, a Rayleigh damping layer is placed above the height of two vertical wavelengths (12.57 km). The wave absorption coefficient

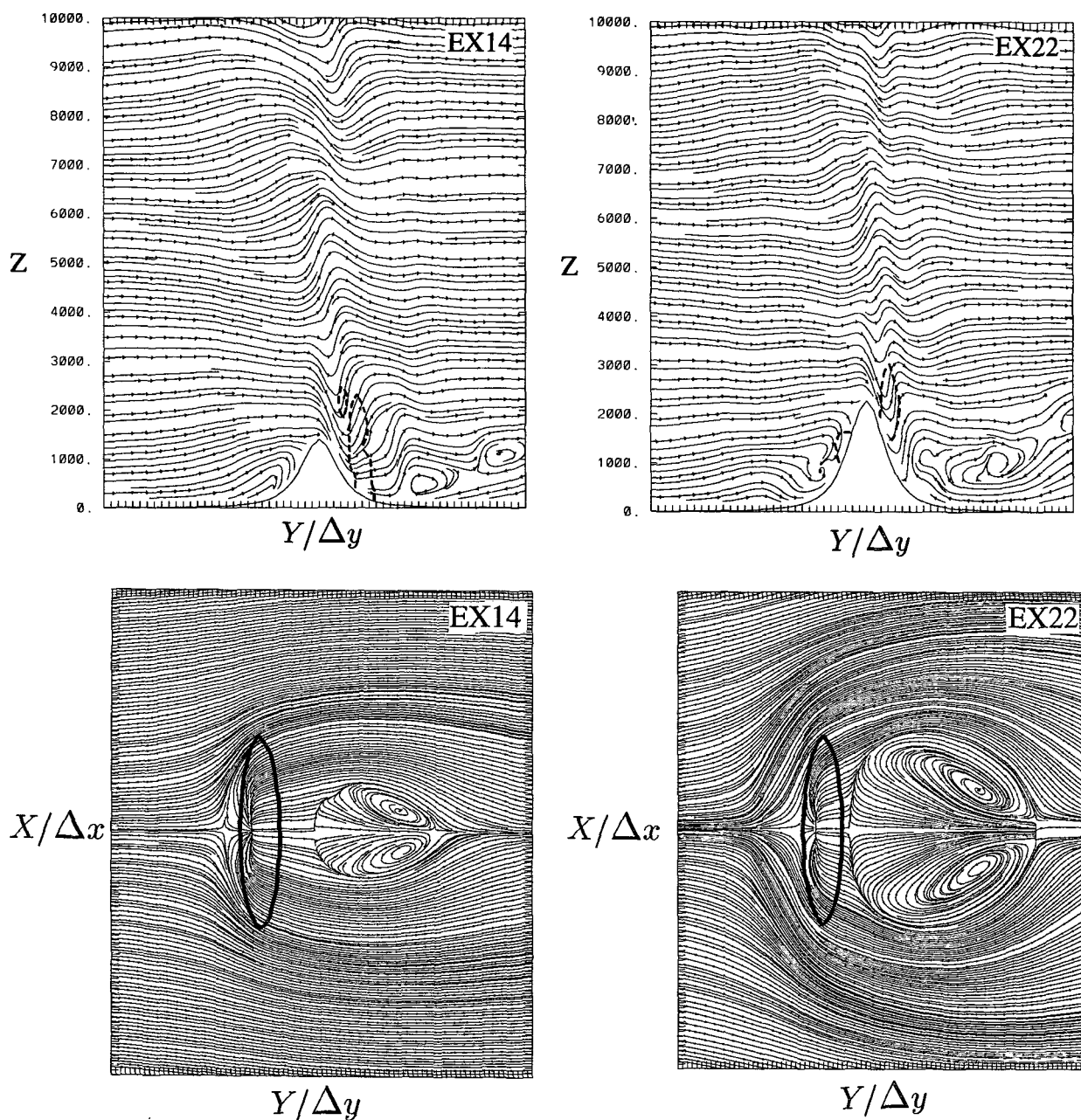


FIG. 2. (Continued)

increases with altitude, according to Klemp and Lilly (1978).

In less than 10 nondimensional time units ($t^* = Ut/L_y$), where L_y is the mountain half-width along the flow, most low-level features of the flow have reached stationarity. The lee vortices continue however to develop, as we shall discuss later in this paper.

The vertical component of the group velocity of the mountain waves can be expressed by $c_{gz} = U^2 k^2 / [N(\sqrt{k^2 + l^2})]$ [see Smith 1980, Eq. (28c)],

where k and l are horizontal wavenumbers. According to Smith, waves with $k \gg l$ propagate vertically, and their wave energy will be found directly above the mountain, while waves with $k \approx l$ will propagate upward, outward, and downstream. Setting $l = 0$ and $k = L_y^{-1}$, we find that it takes 12.6 nondimensional time units for the wave energy to reach up two vertical wavelengths. In fact, we find that the waves just below the absorbing layer continue to grow during this period.

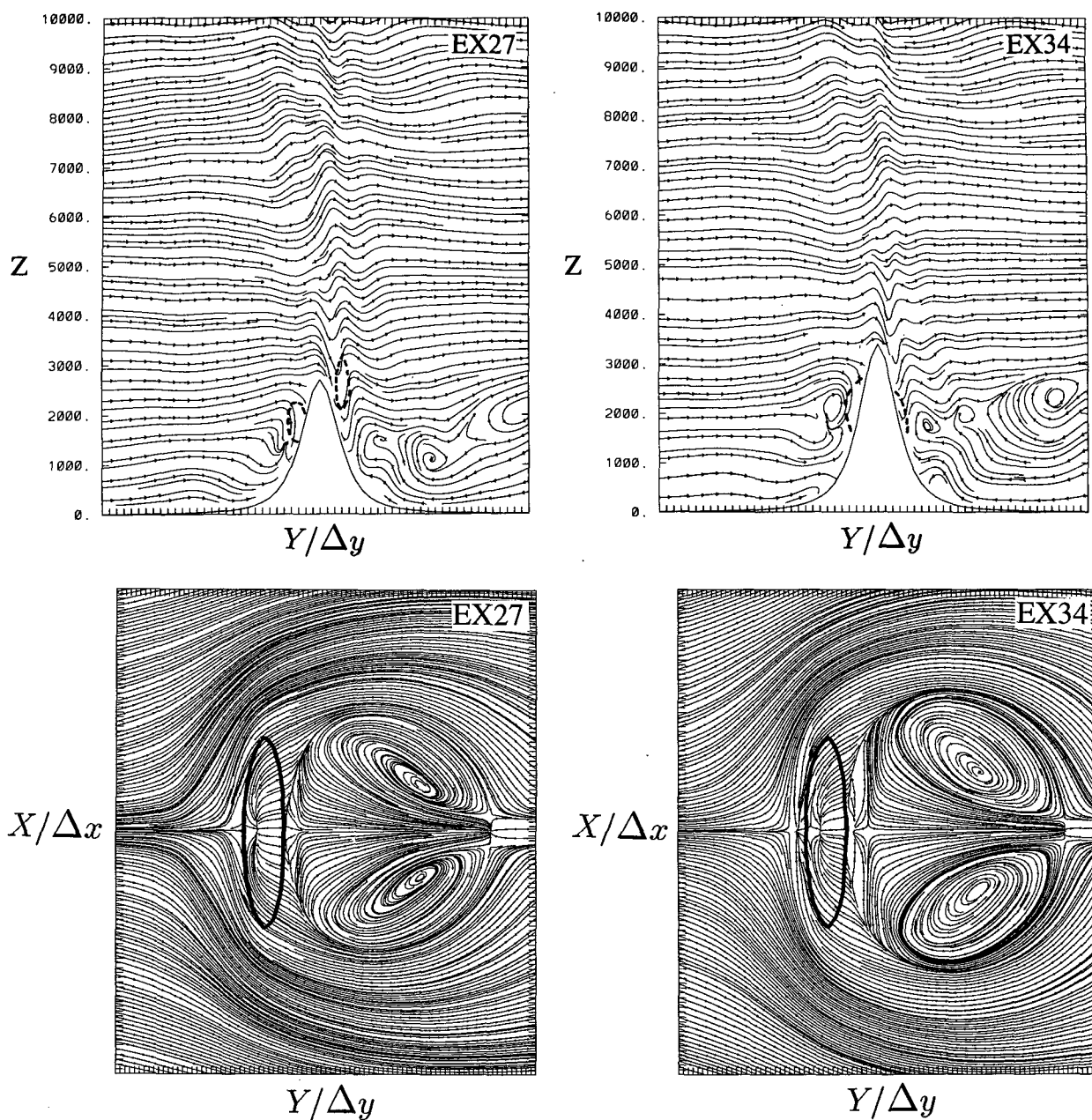


FIG. 2. (Continued)

In the following sections, we discuss results at $t^* = 16.2$, unless otherwise stated. At that time, the flow is sufficiently stationary for our purposes.

The nondimensional mountain height Nh/U is changed through h . Thus, high Nh/U goes together with a high mountain. Keeping L_x and L_y constant, we therefore also get a steeper mountain as Nh/U is increased. Dimensional analysis of Eq. (1) reveals dependence on a horizontal length scale, and the Nh/U similarity is strictly not valid for the turbulence

scheme. This does not seem to have much affect on the results of the present study, since by comparing EX45 and EX45NT, we find that the introduction of turbulence does not lead to morphological changes in the flow. Maximum values of wind speed are reduced in some places in EX45, but all major phenomena, such as the division between the horizontal and vertical flow, the steepening of the mountain waves, and the potential vorticity (PV) field, remain largely unaffected.

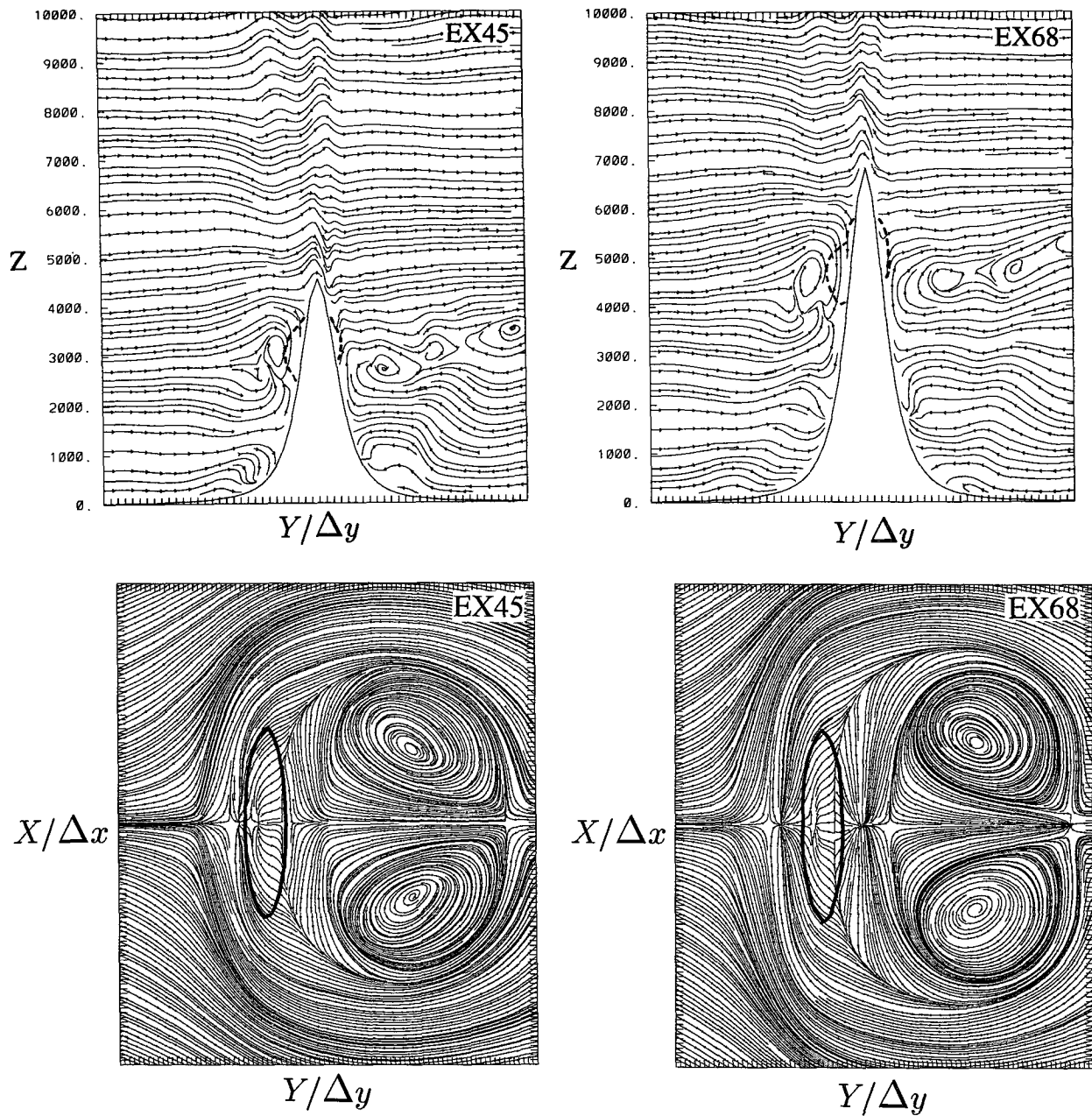


FIG. 2. (Continued)

Although the main features of the flow have reached a stationary state at $t^* = 16.2$, we still observe some fluctuations in the values of some variables in the flow, such as surface pressure and potential vorticity. This may relate to the quasi-stationary nature of wave breaking, which oscillates between the phases of wave buildup and breaking. Other processes in the flow, such as small vortex development in the blocking, may also have a quasi-stationary, oscillating nature. The aim of

this paper is not to study such oscillations but features of the flow that can be regarded as stationary and in particular their dependence on Nh/U .

c. Validation of the simulations

Our first validation was to verify if the model reproduced the expected Nh/U similarity. Without the sub-grid turbulence, we were able to reproduce a good sim-

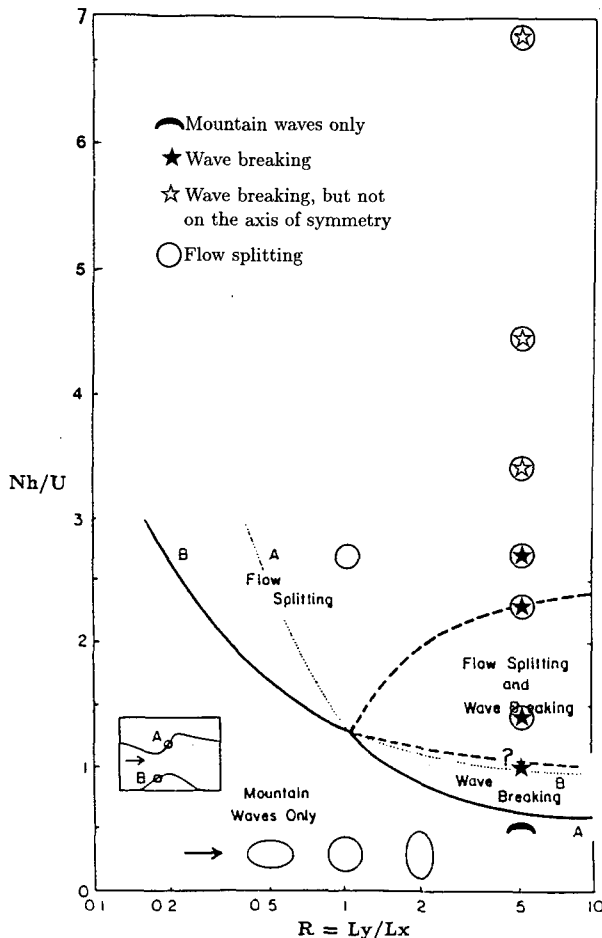


FIG. 3. The simulations presented in this paper transposed on Smith's (1989a) regime diagram. The diagram defines the flow regime as a function of Nh/U and aspect ratio (R). Curve A shows the limits of stagnation aloft (wave breaking), while curve B shows the limits of stagnation on the windward slope (flow splitting). Curves A and B are dotted where linear theory is technically invalid. Dashed lines are Smith's suggestions of critical values for flow splitting and wave breaking within the nonlinear regime. As illustrated by this figure, our results call for a revision of the position of the upper dashed line.

ilarity in simulations where Nh/U was kept constant, but with a different combination of N , U , and h . (EX45NT was compared with a simulation with $N = 0.1414 \text{ m s}^{-1}$, $U = 7.07 \text{ m s}^{-1}$, and $h = 2273 \text{ m}$.) Similar experiments were carried out with the turbulence scheme. In these experiments, the similarity was not as good, but differences due to different combination of N , U , and h nevertheless remained small compared to the differences obtained when varying Nh/U or the aspect ratio.

Then, we compared simulations where $Nh/U = 0.05$ with analytic linear solutions obtained by Smith (1980) for a circular mountain and by Phillips (1984) for an elliptical mountain ridge. The differences between the

theoretical values of the mountain-induced pressure anomalies and the corresponding maximum gridpoint values are within 15% for the circular mountain and within 11% for the elliptical mountain ridge. The parabolic structure of the vertical displacement field and its change with altitude were reproduced nicely in our simulations.

Finally, for $Nh/U = 4.545$ we compare EX45c to the studies of SR (1989, 1990) of flow past a circular mountain. They simulated flow with high Nh/U (low Froude number) and found its morphology to be in good agreement with the laboratory experiment of Hunt and Snyder (1980). EX45c also reproduces this morphology, including stagnation points, upstream flow reversal, and lee vortices. Table 2 compares values of different parameters in SR (1989, 1990) and EX45c. Smolarkiewicz and Rotunno (1989, 1990) found the flow to be essentially steady at nine nondimensional time units. This is also the case for our simulations, except for some parameters related to the lee vortices. Figure 1 shows streamlines in a vertical cross section along the axis of symmetry in EX45c at $t^* = 8.1$ and $t^* = 16.2$. The deep upstream blocking and the weak vertical wave pattern in EX45c and SR (1989, their Fig. 3c) are very much alike. The lee flow in EX45c at $t^* = 8.1$ is similar to SR (1989), but the lee vortices have not reached a steady state and are advected further downstream, which is consistent with the advection of the second downstream saddle point in Table 2. In general, the agreement between SR (1989, 1990) and EX45c is satisfactory, and we have confidence in our model and the numerical setup. Some of the results presented in this paper, such as the flow within the wave breaking regions, may depend on the numerical resolution. However, our simulations reproduce quite well the flow features observed by SR (1989, 1990), who used a better resolution in their study of the low-level morphology. In our study of aspect ratio and Nh/U dependence, we present a better resolution than SR. Yet, our results do not differ significantly from theirs. An extended version of the results of our numerical calculations can be found in Ólafsson (1996).

3. Flow regimes

An overview of the streamline pattern in the simulations is given in Fig. 2. For our lowest value of Nh/U , the kinetic energy of the flow is sufficient for the low-level flow to climb the mountain and create a smooth mountain wave above it. There is, in other words, neither flow splitting defined by stagnation on the windward side of the mountain nor is there stagnation aloft leading to wave breaking. Increasing Nh/U to 1.0 (EX10) gives stagnation aloft and wave breaking above the lee slope. In EX14 the flow features wave breaking, as well as reverse flow on the upstream slope. The latter is a result of surface stagnation. Both stagnation on the surface as well as aloft are predicted by

the linear theory of Smith (1989b). Figure 3 shows our simulations transposed on Smith's (1989a) regime diagram. We see that the flow regimes in EX05, EX10, and EX14 are in agreement with the predictions of linear theory. For higher values of Nh/U , the linear theory is no longer useful since the flow is highly nonlinear. The high- Nh/U theory of Drazin (1961) describes the flow mainly as confined to horizontal planes, and we observe that for increasing Nh/U an increasing proportion of the flow is diverted horizontally rather than vertically (see Table 1, line 7). Drazin's (1961) theory is nonetheless of limited use in our study since it describes flow around a circular obstacle and does not allow for vertically propagating gravity waves. Smith (1989a) has suggested an upper limit for wave breaking. This limit is indicated in Fig. 3 by a dashed line separating the regions of flow splitting and wave breaking and flow splitting on the regime diagram. According to Smith, the position of this line is not yet known. As shown in Fig. 3, all our simulations with $Nh/U \geq 1.4$ and $R = 5$ give wave breaking, and, consequently, they do not reveal an upper critical value of Nh/U for wave breaking. This may be the main result of this study. However, we note that for $Nh/U \geq 3.4$ the wave breaking does not occur any longer on the axis of symmetry but is limited to narrow regions on either side of the mountain (see also Fig. 14). Thus, by displacing the dashed curve upward on Smith's regime diagram, it may become useful for predicting wave breaking on the axis of symmetry, while the upper limits of overall wave breaking for aspect ratio 5 remain unexplored.

4. Upstream blocking

Apart from Smith's (1989a) linear theory, stagnation is observed in experimental studies (Hunt and Snyder 1980; Baines 1987) and in several numerical studies, such as SR (1990). Baines (1987) describes the upstream blocking as a wave phenomenon that propagates upstream as columnar motions that permanently alter the density and horizontal velocity profiles. Pierrehumbert and Wyman (1985) have also carried out numerical studies of upstream effects. For a nonrotating case, they found the decelerated layer to propagate arbitrarily upstream, while for a rotating case this is not so; the upstream blocking quickly reaches a maximum before retreating to a less decelerated value.

Stagnation on the windward slope is indeed present in all our simulations with values of $Nh/U \geq 1.4$. Most of the air mass that meets the mountain is decelerated and partly reversed. We shall call this mass of decelerated air together with the reversed flow *upstream blocking*. In our simulations, the blocking continues to grow beyond 20 nondimensional time units. In their studies, Pierrehumbert and Wyman (1985) used an infinitely long mountain ridge, while in our case the mountain ridge is finite, and the flow can pass on each

side of it. However, in view of Pierrehumbert and Wyman's (1985) results we may expect the upstream extension of blocking to be affected by the distance between the upstream boundaries and the mountain. We will therefore not discuss this aspect of our simulations. The results close to the mountain appear not to be affected by this possible problem, and we note for instance that the position of the upstream saddle point is in perfect agreement with SR (1990) (see Table 2), which used a larger domain.

Most papers on stagnation and upstream blocking describe a kinematic pattern of two singular points in the surface flow. Close to the mountain top, a streamline following the axis of symmetry splits and a singular surface point is formed. In Fig. 4a, this point is referred to as S'_u . The streamline that ends in S'_u divides the flow into two parts. One part of the flow ascends the mountain, and the other part returns and flows down the upstream slope. Farther down the upstream slope, where this return flow meets the upstream flow, another singular point is formed (S'_l). This point is sometimes referred to as a "separation point." Using the topolog-

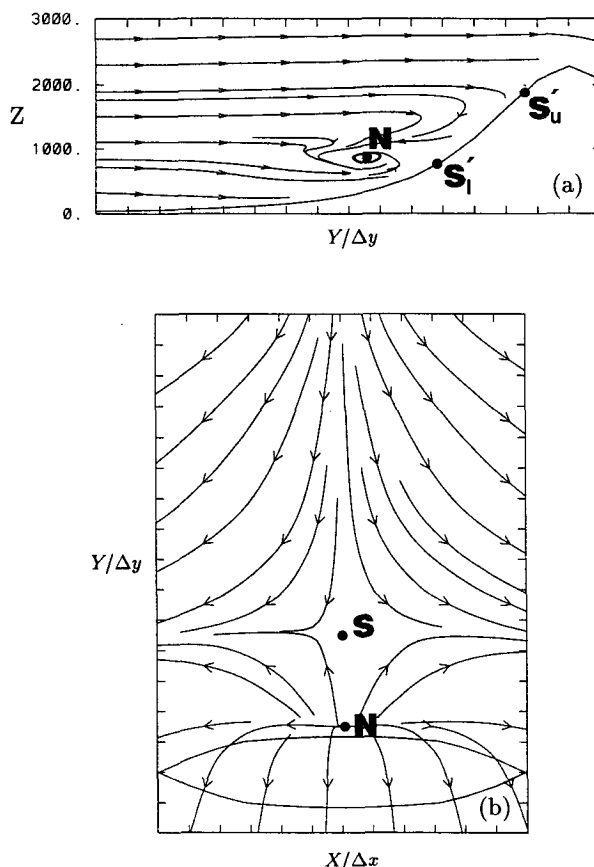


FIG. 4. Singular points upstream of the mountain in EX22. (a) A vertical cross section on the axis of symmetry. (b) The surface flow. The symbol **N** represents a nodal point, **S** a saddle point, and **S'** a half-saddle.

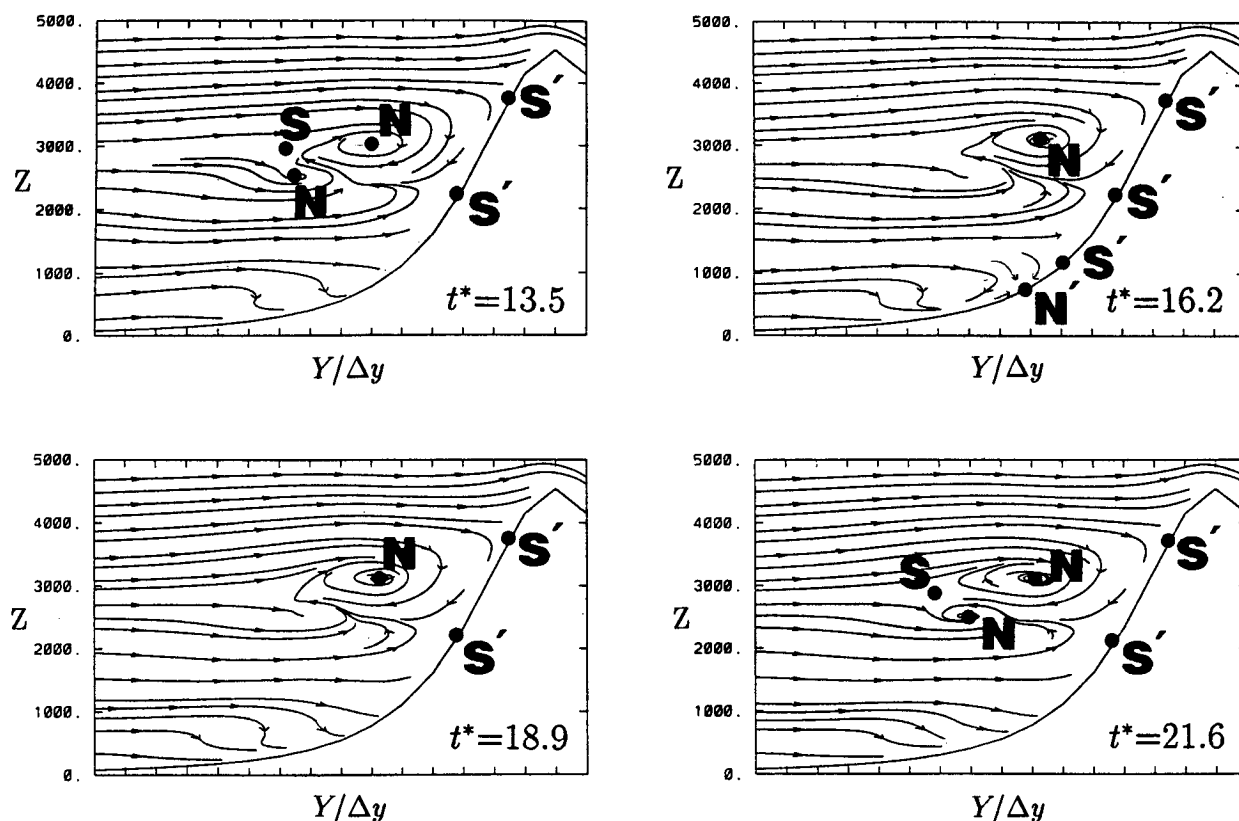


FIG. 5. Singular points upstream of the mountain at 13.5, 16.2, 18.9, and 21.6 nondimensional time units. The panels show vertical cross sections on the axis of symmetry in EX45. The symbol **N** represents a nodal point, **S** a saddle point, **N'** a half-node, and **S'** a half-saddle. The flow is from left to right.

ical terminology of Hunt et al. (1978), both points would be classified as half saddles in a vertical plane, but in a horizontal projection of the surface flow, the former point would be classified as a nodal point (**N**) and the latter as a saddle point (**S**) (Fig. 4b).

According to Hunt et al. (1978), a simply connected flow is kinematically impossible unless there is an equal number of nodal and saddle points in all two-dimensional plane sections of the flow [two half-saddles (half-nodes) count as one saddle (nodal) point]. In our simulations, the flow follows this rule, as can be seen in Figs. 4a,b. A close study of the panels of surface flow in Fig. 2 shows in some cases not two, but four singular points ($2S + 2N$) in the upstream surface flow. Table 1 (lines 2 and 3) shows that there is a broad tendency for increase in the number of singular points with increase in Nh/U . The tendency for more singular points in flow with high value of Nh/U is presumably related to the fact that in these cases the blocking is of the greatest vertical extent, allowing for a more complex flow pattern. Small vortices may appear and disappear inside the blocking, and when they are connected to the surface, additional singular points form in the surface flow upstream of the mountain. A pattern

of four singular points in the surface flow can also be observed in SR's (1990, their Fig. 11) simulation with $R = 8$ and $Nh/U = 3$ ($Fr = 0.33$).

Although the main features of the flow are stationary, the total number of singular points in the surface flow is not stationary. We find for instance that the total number of singular points on the windward surface in EX45 is only 2 at 13.5, 18.9, and 21.6 nondimensional time units, while at $t^* = 16.2$ we have four points, as shown in Table 1. Figure 5 shows the time evolution in a vertical plane. In Fig. 5b at $t^* = 16.2$, we have two additional singular points at the surface. These points are related to slow return flow at the surface in a limited area upstream of the separation point (S'_1 in Fig. 4a). At all times, there is however one major horizontally oriented vortex that is stationary. At $t^* = 13.5$ (Fig. 5a), we find a small vortex below the major vortex. At $t^* = 16.2$ (Fig. 5b), this vortex has disappeared, but at the end of the simulation, at $t^* = 21.6$, (Fig. 5d) it reappears. This vortex remains aloft, and, consequently, it does not affect the number of singular points at the surface.

In general, after the onset of stagnation on the windward side of the mountain, the additional singular

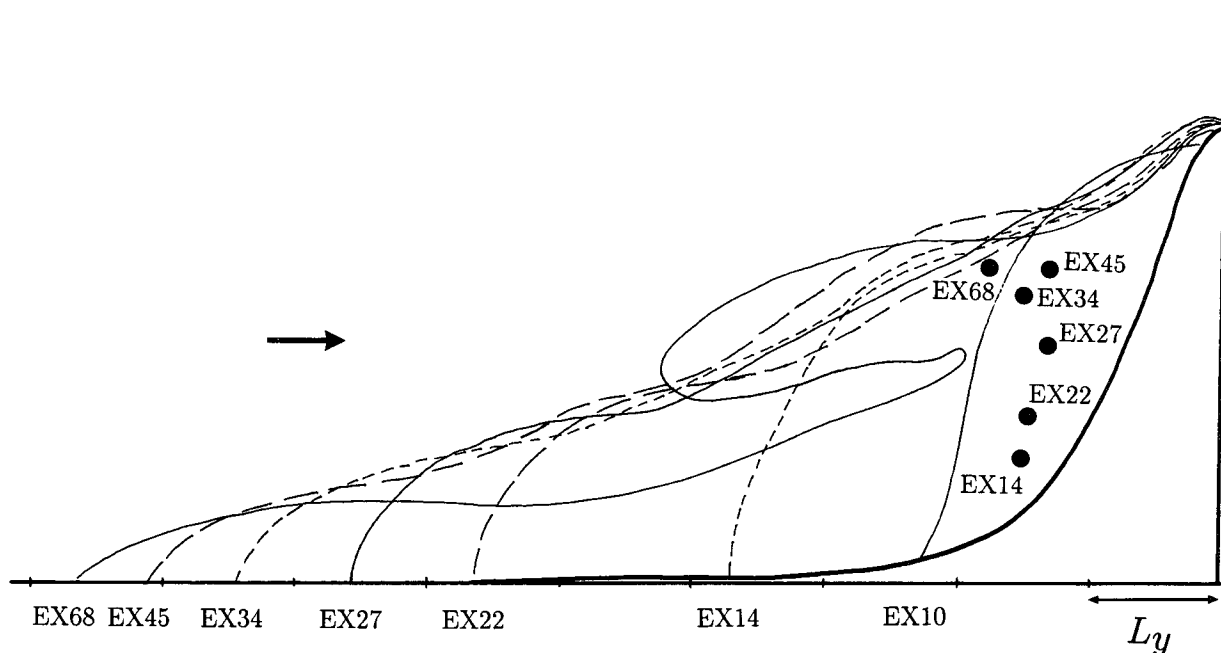


FIG. 6. Isolines of $u = 0.5U$ and position of the nodal point in the major horizontally oriented vortex inside the upstream blocking. The nondimensional mountain height has been normalized with the mountain height in each case, and the mountain top is located at the right edge of the frame. The flow is from left to right.

points on the surface, or in a vertical cross section, do not seem to relate to major changes in the flow.

A study of blocked, real flow from PYREX has revealed a tendency for not only two, but multiple, singular points in the upstream blocking. Such a complex flow pattern is simulated both with and without surface friction.

All our simulations with flow splitting show one major, horizontally oriented vortex inside the blocking. This vortex becomes larger as Nh/U is increased, as can be seen in Fig. 2. The maximum speed of the return flow in the blocking is found in connection with this main vortex. Table 1 (lines 10 and 11) shows the maximum speed of the reverse flow and the maximum values of turbulence kinetic energy (TKE) in the upstream blocking. A detailed analysis shows that the upstream TKE is mainly generated by the local wind shear. Apart from the relatively low value in EX27, the speed of the return flow increases linearly with Nh/U . Comparing EX45 and EX45c, we find that increasing the aspect ratio from 1 to 5 leads to 3–5 folding of the maximum value of the reverse flow and the turbulence kinetic energy.

Figure 6 shows isolines of $u = 0.5U$ in all our simulations on a cross section along the axis of symmetry. The position of the horizontally oriented vortices is given by black dots. Not unexpectedly, we find that deceleration is much more efficient at lower levels than at levels closer to the mountaintop level. In EX34,

EX45, and especially in EX68 we also note that the isolines have a wavy form around the vortex.

Table 1 (lines 4–6) shows the height of the upper-surface stagnation point h_s (half-saddle in a vertical section, but node in the surface flow) and the upstream height of the isentrope that intersects the mountain at this point. We shall hereafter call this height Z_{0s} (see Fig. 7). A remarkable feature of our simulations accounting for subgrid turbulence is that the height of the upper-surface stagnation point (h_s) is roughly proportional to the mountain height, while Z_{0s}/h increases with increasing Nh/U . A result of this is that a particle following an isentropic streamline starting at Z_{0s} and intersecting the mountain in h_s climbs much more in simulations with low Nh/U than in simulations with high Nh/U . Further study of Table 1 shows that $h - Z_{0s}$ is roughly independent of Nh/U for the range of Nh/U between 1.4 and 4.5, while Z_{0s} increases with increasing Nh/U . Thus, as Nh/U is increased, the pro-

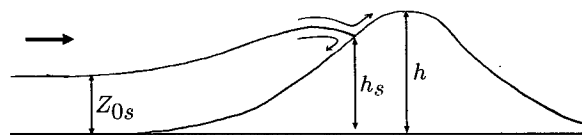


FIG. 7. A schematic figure of the dividing streamline (bold) that intersects the mountain in h_s . The flow is from left to right.

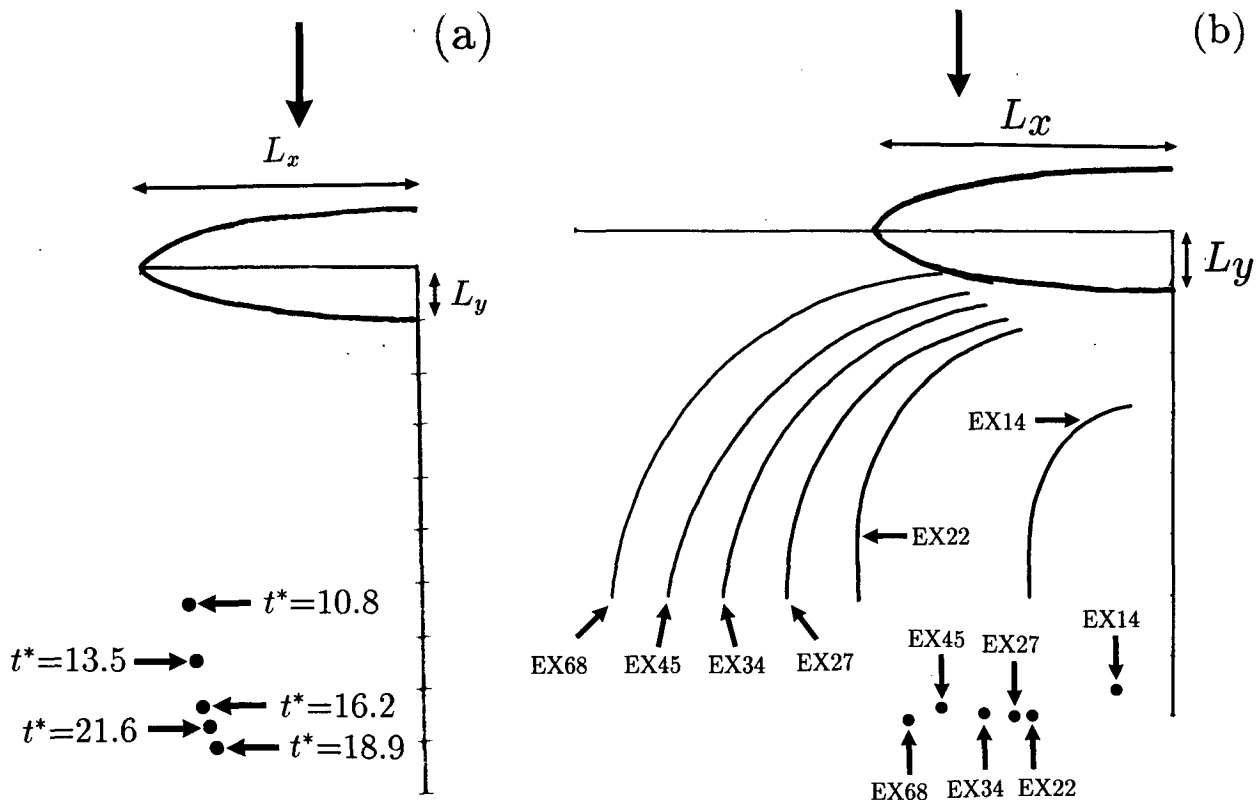


FIG. 8. (a) Lee vortex position at different nondimensional time units in EX45. (b) Position of the shear line and the lee vortex in simulations with different values of Nh/U . The positions in EX45NT are the same as in EX45. The flow is down the page.

portion of horizontally or laterally deviated air is increased. This may be important for the suppression of wave breaking, as we shall discuss later.

We note that, moving from aspect ratio 1 to 5, h_s/h increases from 0.20 to 0.81. This does not mean that for a circular mountain all the flow above $0.20h$ on the axis of symmetry ascends the mountain. A closer look at the flow in EX45 and EX45c reveals that the upstream height of an isentrope intersecting the mountain top is $0.91h$ in EX45c and $0.82h$ in EX45. This leads us to conclude that for a circular mountain the flow above h_s is diverted to both sides to a much greater extent than in the case of a mountain ridge.

Hunt and Snyder (1980) suggested a formula of the form

$$Z_{0s} = h \left(1 - \alpha \frac{U}{Nh} \right), \quad (3)$$

where α is a constant. In laboratory experiments, they found Eq. (3) to be roughly valid for a circular mountain and $\alpha = 1$. We find Eq. (3) with $\alpha = 1.2$ to predict the value of Z_{0s} well for all simulations with $R = 5$ except EX22 and EX68, which show a rather poor fit. Thus, unlike h_s/h , Z_{0s}/h is not constant for constant U and N and increasing h (Table 1). This is in fact not

surprising since no account has been taken for the mountain-induced pressure anomaly when deriving Eq. (3). This is particularly important for mountains with high aspect ratio, which generate greater pressure anomalies than circular mountains (see Fig. 17).

In the case of a circular mountain, Eq. (3) with $\alpha = 1$ gives $Z_{0s}/h = 0.78$. This is far away from the simulated value of 0.20 but consistent with the flow being largely split above h_s . In fact we find the upstream height of the isentrope that intersects the mountaintop ($0.91h$) to be much closer to the predicted value of $0.78h$.

5. Lee vortices

As can be seen on the surface streamlines in Fig. 2, a pair of large vortices is formed in the lee of the mountain ridge for $Nh/U \geq 1.4$. This is in accordance with the results of SR (1989), who found such vortices to exist, even in the absence of surface friction, as is the case in our simulations. The role of bottom friction in the generation of vorticity is studied in a recent paper by Grubišić et al. (1995). They show that the bottom friction in shallow water flow acts only to modify the vorticity generation but that the wake formation is dominated by a pseudoinviscid process related to a hydraulic jump in the lee of the mountaintop. Since our

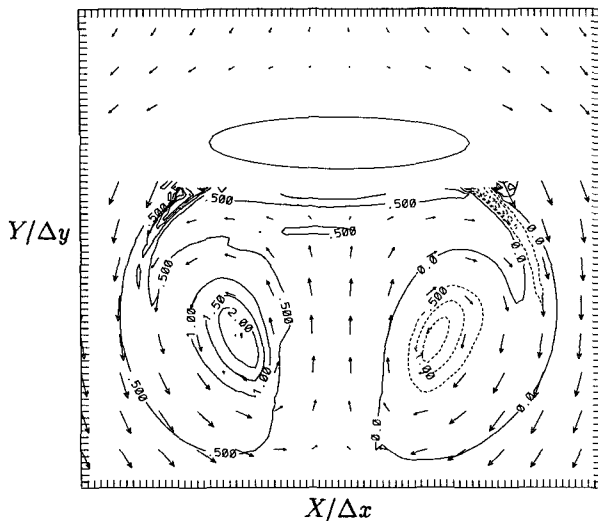


FIG. 9. Wind arrows and potential vorticity at the height of 0.1 h in EX45. The PV is in PV units. The flow is from page top to bottom.

simulated flow is symmetric, we do not expect vortex shedding (SR 1989; Schär and Smith 1993a; Sun and Chern 1994). Following the evolution in time of the vortex centers in EX45 (Fig. 8a), we see that the vortices propagate downstream until they reach a maximum distance from the mountain at $t^* = 18.9$. At $t^* = 21.6$ the vortex centers have retreated a little and are placed in between the positions at $t^* = 16.2$ and $t^* = 18.9$.

The position of the vortices at $t^* = 16.2$ is about 8 mountain alongstream half-widths downstream of the mountain ridge for all values of Nh/U (Fig. 8b). This value may be affected by the size of our simulation domain and should not be taken too literally. On the

other hand, the distance of the vortices from the axis of symmetry varies between approximately 0.2 and 0.8 times cross-stream half-width, placing the vortices in EX14 closest to the axis of symmetry and the vortices in EX68 farthest away from it.

The centers of the lee vortices are at a greatest distance from the axis of symmetry and from the mountain ridge in the surface flow. Moving upward, away from the surface, we find the vortices to be closer to the axis of symmetry and to the mountain ridge. In other words, we may say that a line running through the vortex centers tilts backward and toward the axis of symmetry.

More than one mechanism has been suggested to explain the vorticity generation responsible for the lee vortices (Smith 1989b; SR 1989; Schär and Smith 1993a). Schär and Smith (1993a) show vorticity production to be related to the joining of two streams of fluid with different values of the Bernoulli function. This result is obtained with dissipation and within the shallow-water framework. We note that the downstream traces of potential vorticity in our simulations (Fig. 9) are very much like the vorticity pattern in Schär and Smith (1993a, their Fig. 8). According to Schär and Smith, the joining of the two streams of fluid with different values of the Bernoulli function occurs on the shearline, where the decelerated air in the wake meets the low-level accelerated flow that has been diverted laterally to each side of the mountain. Figure 10 shows the alongstream wind component and the related PV in a vertical cross section perpendicular to the upstream flow, two alongstream half-widths downstream of the mountain. Both the wind shear and the PV are strongest close to the surface and decrease quite rapidly with altitude in the lowest hundreds of meters. Not surprisingly, both fields reproduce the form of the mountain and tilt with height toward the axis of symmetry. Table 1 (line 15) shows that the PV concentration on

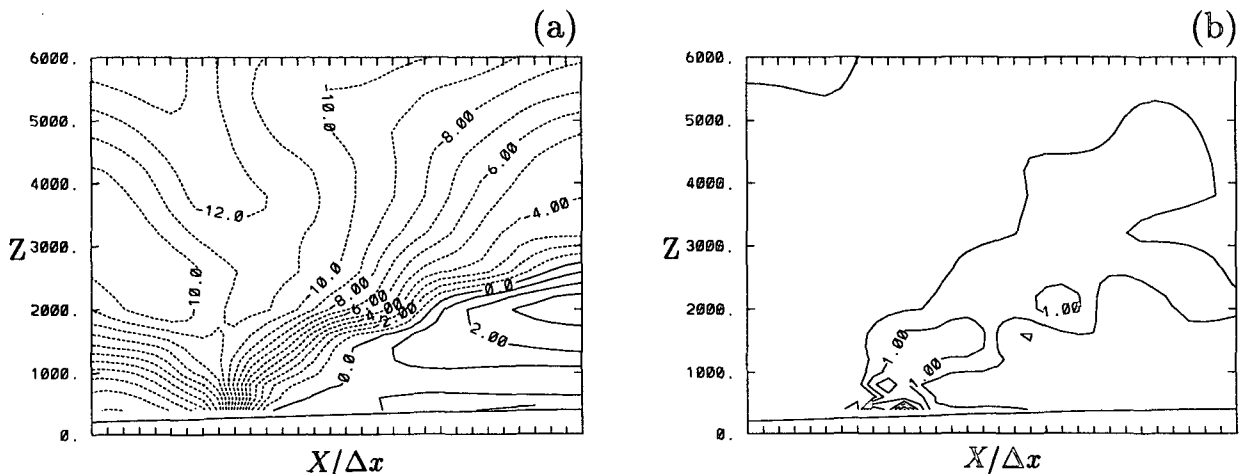


FIG. 10. Vertical cross section across the flow 1 alongstream half-width downstream of the mountain in EX45. The axis of symmetry is at the right edge of each frame. (a) Wind speed out of the plane in m s^{-1} , and (b) potential vorticity in PV units with isolines of 0.5 PV units.

the shearline increases rapidly close to the onset of stagnation on the windward slope. For higher values of Nh/U , our simulations do not reveal a clear Nh/U dependence on the shearline.

The potential vorticity generated close to the mountain seems to be advected along the shearline and into the lee vortices. In the centers of the lee vortices, a second maximum is observed in simulations with $Nh/U > 1.4$. Table 1 (lines 13 and 14) shows PV values in the lee vortices at $0.1h$ and at 100-m height. At $0.1h$ the PV values remain stable for Nh/U , ranging from 2.273 to 3.400, and then increase. At 100 m, the PV increases more regularly from EX22 to EX45, but EX68 gives a value similar to EX45. The fact that we observe an Nh/U -dependent increase of PV in the vortices, but not as clearly on the shear line, may be explained by the shear line PV being advected away more rapidly by the faster flow at high Nh/U .

Another closely related, possible mechanism of vorticity generation is through creation of turbulence related to wave breaking or associated with singular points in the upstream flow. As shown in Table 1, an increase in the maximum value of turbulence kinetic energy on the upstream side goes together with an increase in potential vorticity on the lee side. We have tested the role of turbulence in the PV generation by running EX45 without the turbulence scheme (EX45NT). This resulted, in fact, in an increase in the PV on the lee side, presumably caused by the faster flow (see Table 1, line 17), giving stronger PV generation on the shearline. If the turbulence scheme was responsible for the PV generation, one would have observed less PV in EX45NT than in EX45. We are led to conclude that the dissipation due to the turbulence scheme is small compared to other dissipative mechanisms in our model, namely the horizontal diffusion and the discretization errors. This is also supported by a close inspection of the behavior of the other experiments. For increasing Nh/U , dissipation created by the turbulence scheme decreases but PV increases (not shown). In fact, the greatest increase in PV concentration occurs at the onset of flow splitting and not at the onset of wave breaking. Dissipation related to the wave breaking is however an order of magnitude greater than in the upstream blocking. This calls for further study of PV generation in uniformly stratified flows.

We may note that by removing the turbulence parameterization (EX45NT) we did not produce any major morphological changes in the flow; the vortices are slightly deformed, but their position remains unchanged.

Smolarkiewicz and Rotunno (1989) observed the height (depth) of the lee vortices decreasing with increasing Nh/U for $R = 1$. Table 1 (line 16) reveals a similar tendency for $R = 5$, but in EX68 the vortices still reach up to $0.78h$. A comparison between EX45 and EX45c shows a 60% increase in the height of the vortices as the aspect ratio goes from 1 to 5. Further comparison between these two simulations shows

about a 40% increase in the lee return flow and the concentration of shearline PV for the mountain ridge.

6. Areas of accelerated flow

Figure 11 from EX45 and EX45c shows the horizontal wind speed in vertical cross sections across the flow. The axis of symmetry is at the right edge of each frame. The cross section in Fig. 11a is taken as 1.5 alongstream half-widths upstream of the mountaintop in EX45, and in Figs. 11b–d we move downstream with steps of 1 alongstream half-width. In Fig. 11a we note a closed core of accelerated air at about 5000-m height. We shall call this the upper area of accelerated flow. In Fig. 11b the upper area of accelerated flow has moved a little downward and away from the axis of symmetry. A second maximum has appeared at about 2000-m height and is a little farther away from the axis of symmetry. We shall call this the lower area of accelerated flow. In Fig. 11c we have passed the mountain ridge. The upper area of accelerated flow has disappeared, and the lower area of accelerated flow appears now as an extension of a surface windstorm. In Fig. 11d the surface windstorm has moved away from the axis of symmetry and forms a shearline with the slow flow in the wake.

Let us now look at the flow on an isentropic surface, viewed from above. Since surface friction, radiation, and latent heating are neglected, the flow is close to isentropic except where the isentropes turn over and turbulent mixing becomes important. This happens mainly in upstream vortices and where mountain waves break. Thus, we can expect streamlines on an isentropic surface to represent trajectories fairly well.

Figure 12a shows a streamline in EX45 on an isentropic surface whose upstream height is close to h , the mountain height. At this isentropic level we are situated above the blocking, and there is no deceleration in the flow. Following the streamline, we enter into the upper area of accelerated flow, whose maximum speed is reached approximately one half-width away from the axis of symmetry.

Moving downward, we find in Fig. 12b a streamline on an isentropic surface whose upstream height is about $h/2$. At this level the streamline enters into the lower area of accelerated flow, which is larger than the upper area of accelerated flow. The lower area also features stronger wind speed and extends downstream of the mountain crest. By following the streamline, we find that the flow that acquires greatest wind speed originates from within the blocking, where it has been strongly decelerated before escaping the blocking. Indeed we find by tracing streamlines on this isentropic surface that the faster the flow reaches its maximum, the greater its deceleration has been inside the blocking.

On an isentropic surface whose upstream height is about $h/4$ (Fig. 12c), we find that the area of accelerated flow and maximum wind speed has still in-

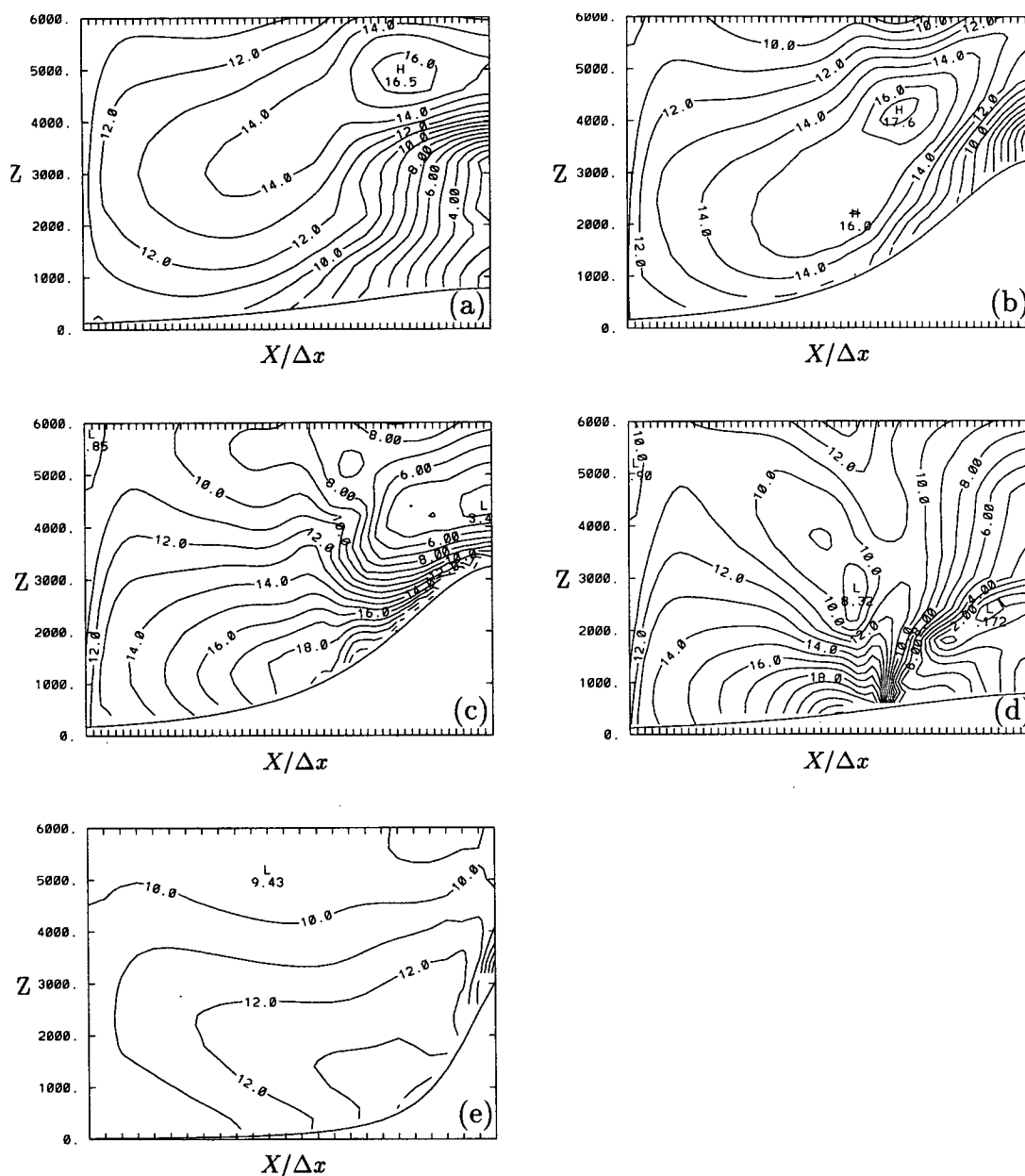


FIG. 11. Vertical cross sections across the flow, showing wind speed in meters per second in EX45: (a) 1.5 alongstream half-widths upstream of the mountain, (b) 0.5 alongstream half-widths upstream of the mountain, (c) 0.5 alongstream half-widths downstream of the mountain, (d) 1.5 alongstream half-widths downstream of the mountain, and (e) the wind speed 0.5 alongstream half-widths upstream of the mountain in EX45c.

creased and moved farther downstream. As in Fig. 12b, the accelerated air comes mainly from within the upstream blocking.

Figure 12 also shows the geopotential height of the isentropic surface. We see that in all cases a wind speed value of $1.6U$ is reached shortly after the flow has passed the wave crest and started to descend. In Fig. 12a, where the initial height of the isentrope is about 4550 m (h), a maximum wind speed of $1.7U$ is reached

after a descent of about 400 geopotential m, but in Figs. 12b,c, where the initial heights of the isentropes are about 2260 m ($h/2$) and 1230 m ($h/4$), the flow descends about 1000 geopotential m and accelerates much more. In both cases we note that the maximum wind speed is reached after the steepest descent and just before the flow has reached the bottom of the wave.

A closer study confirms that the upper area of accelerated flow, which is displaced downward and away

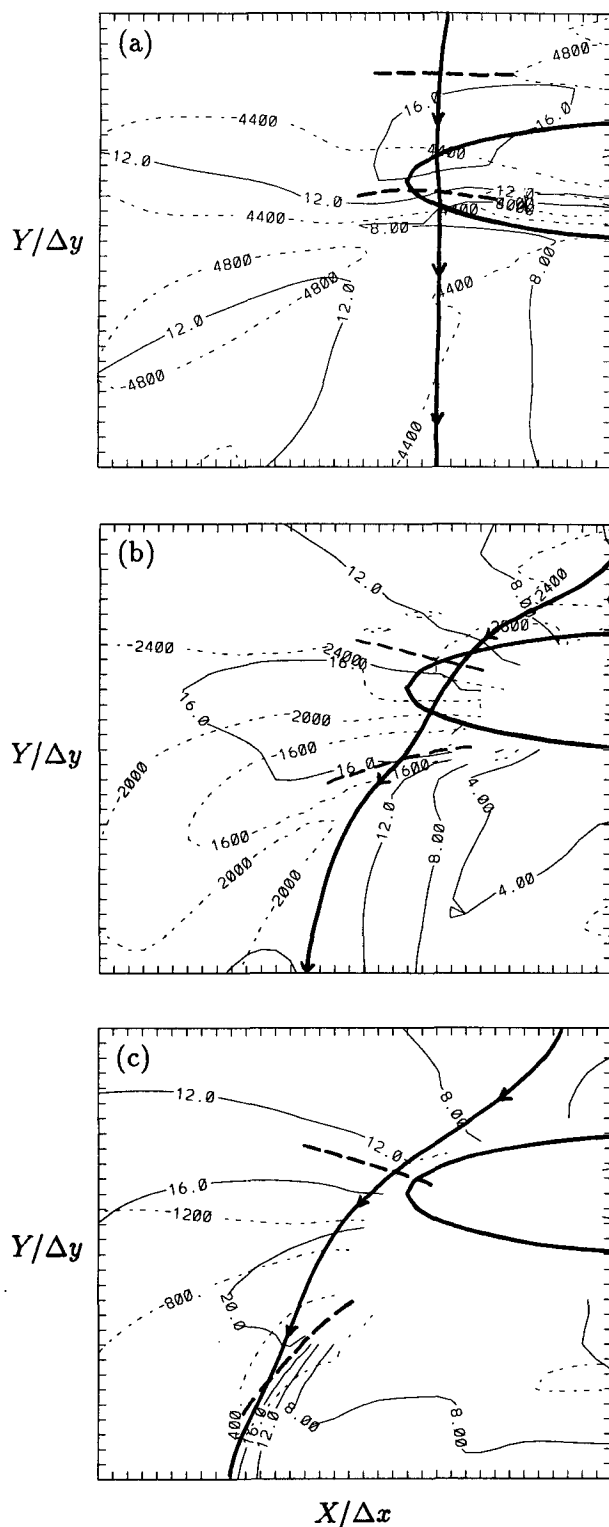


FIG. 12. Wind speed (in m s^{-1}) (solid lines), one streamline, and the geopotential height (dashed lines) of isentropic surfaces in EX45. (a) Isentropic surface at 299 K, whose upstream height is about h . (b) Isentropic surface at 292 K, whose upstream height is about $h/2$. (c) Isentropic surface at 288 K, whose upstream height is about $h/4$. The wave crests and bottoms are indicated with a bold dashed line.

from the axis of symmetry as it approaches the mountain ridge, has its area of maximum wind speed everywhere aloft and does not touch the ground. The lower area of accelerated flow stays, on the other hand, aloft only a short distance. It descends and joins a surface wind maximum. In EX68, this happens before the flow reaches the crest of the mountain ridge, while in the other simulations the core of maximum wind speed joins a surface windstorm a short distance downstream of the crest.

In EX45 and EX68 the upper area of accelerated flow is separated in space from the lower area of accelerated flow. In the other simulations with lower value of Nh/U , this is not so. In these cases a core of accelerated flow runs smoothly downward and farther away from the axis of symmetry as it approaches and passes the mountain ridge.

The maximum values of the wind speed in the upper areas of accelerated flow are close to $1.8U$ and they are quite independent of Nh/U . On the other hand, we find the height of these areas of accelerated flow to be proportional to mountain height. Table 1 (lines 17 and 18) shows the overall maximum wind speed and the maximum wind speed on the axis of symmetry. In cases with $Nh/U \geq 2.273$, the overall maximum wind speed is not on the axis of symmetry but in the surface windstorm that is connected to the areas of accelerated flow. The maximum wind speed in the surface windstorm increases for increasing Nh/U , but slowly. The position of the windstorm moves away from the axis of symmetry for increasing Nh/U as can be seen on Fig. 8b, which shows the associated shearline.

We expect that both the accelerated flow on the windward side and on the lee side of the mountain ridge is created by the mountain-induced pressure anomaly, directly or indirectly through the upstream blocking. The location of the upstream accelerated areas indicates that they are a result of flow deflection on both sides of the blocking. One may therefore expect the structure of the blocking to be of significant importance in forming at least the upper areas of accelerated flow. Since the lower areas of accelerated flow are fed by air that escapes the blocking by flowing around the edges of the mountain ridge, we expect the mountain shape to affect the structure and even the intensity of the lower-level accelerated flow. Through the blocking, the mountain shape can also be expected to affect indirectly the structure of the upper areas of accelerated flow.

Figures 11b and 11e show the flow past a mountain ridge with aspect ratio 5 and flow past a circular mountain. In EX45c we find the flow to be accelerated but much less so than in the mountain ridge case. Comparing EX45 and EX45c in Table 1 yields similar results: about a 30% increase in maximum surface wind and about a 60% increase in maximum surface wind on the axis of symmetry for the mountain ridge.

7. Wave breaking

a. Theory and detection of wave breaking

When the steepening of a mountain wave reaches a critical value, the wave overturns or breaks, and the air becomes convectively unstable. As discussed before, the three-dimensional linear theory of Smith (1989b) predicts stagnation aloft above the mountain, leading to wave breaking. The positive effect of reversed wind shear on wave breaking has been known for a long time (Förchgott 1949) and has been confirmed theoretically by Smith (1989b). For a given mountain shape, numerical simulations by Smith and Grønås (1993) and others have confirmed the theoretical results of the onset of wave breaking as Nh/U passes a critical value, depending on the mountain aspect ratio. The critical value for a bell-shaped mountain with aspect ratio just exceeding 1 is a little more than 1 but decreases as the mountain aspect ratio increases. As Nh/U increases and with the onset of stagnation on the surface as well as aloft, linear theory becomes technically invalid and is unable to predict an upper critical value for Nh/U . For a high value of Nh/U , one may expect most of the flow to be diverted horizontally. This is indeed so; for increasing Nh/U , an increasing portion of the flow (Z_{0s}/h in Table 1) is diverted horizontally, rather than vertically. However, we observe in our simulations that for all values of Nh/U a substantial part of the flow is still diverted vertically rather than horizontally [$(h - Z_{0s})/h$ in Table 1]. This will be discussed later in this paper.

In our simulations, wave breaking is detected by a high concentration of turbulence kinetic energy related to maximum steepening of potential temperature fields. This maximum is obtained where the air is rising after having passed the bottom of the wave. Due to turbulent mixing, complete stagnation in general does not occur in our simulations. In other words, the flow is not reversed but becomes very slow ($0\text{--}2\text{ m s}^{-1}$) in the wave breaking region. At the onset of wave breaking, the turbulence kinetic energy increases significantly, reaching a typical value of $1\text{--}5\text{ m}^2\text{ s}^{-2}$. Figure 13 illustrates

the effect of the subgrid turbulence $0.5L_x$ away from the axis of symmetry in flow with $Nh/U = 1.4$. Figure 13a shows flow with the turbulence scheme active, while Fig. 13b shows the same situation but with no turbulence scheme. Clearly, the isentropes are reversed in Fig. 13b, while in Fig. 13a they are only vertical. The region where the isentropes are vertical in Fig. 13a has a significant concentration of turbulence kinetic energy.

b. Regions of wave breaking

As previously stated, wave breaking is observed in all of our simulations with $R = 5$ except for EX05. On the other hand, EX45c has no wave breaking. Figure 14 shows the horizontal extension of the wave breaking areas. In EX10, which is close to the critical limits of wave breaking predicted by Smith's (1989b) linear theory, the wave breaking is confined to an area that extends horizontally only a short distance away from the axis of symmetry. Moving to higher values of Nh/U , wave breaking spreads all along the lee slope, and in EX22 and EX27 the wave breaking areas extend as far as 1 cross-stream half-width on each side of the axis of symmetry. In EX34, as well as in EX45 and EX68, there is wave breaking only in isolated areas on each side of the axis of symmetry but not on the axis itself. Figure 15 shows a schematic perspective of the flow in EX45. The wave steepening on each side of the axis of symmetry is shown by an isentropic level whose up-stream height is about $1.1h$.

We choose to classify regions of maximum wave steepening as shown in Fig. 16: **a** is at a low level above the lee slope, **b** is at a higher level and above the mountain top or the upstream slope, and **c** is about one vertical wavelength above **a**. Maximum steepness and possible wave breaking could also be expected one vertical wavelength above region **b**. This is, however, hindered by the wave absorbing layer, which is located above 12.57 km. The wave breaking in EX14, EX22, EX27, EX34, and EX45 is only detected at a low level above the lee slope in region **a**, while in EX68 wave breaking is found at **b** and **c** as well. Steepening occurs,

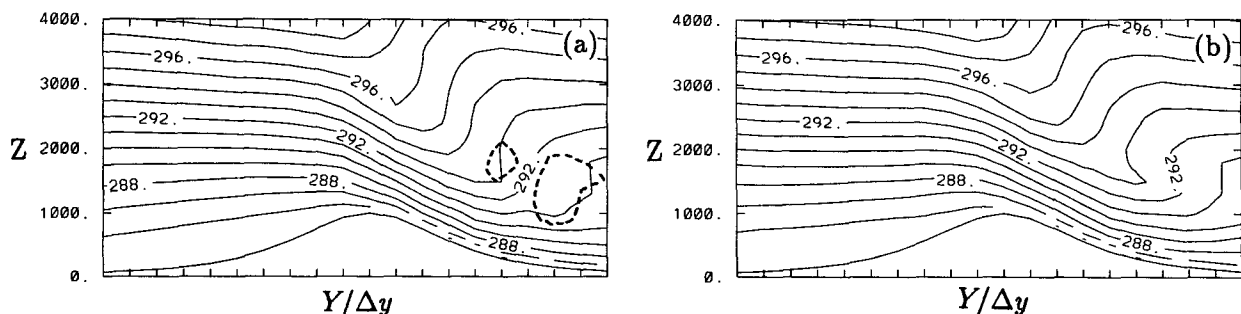


FIG. 13. A cross section of isentropes one $0.5L_x$ from the axis of symmetry in EX14: (a) with the turbulence scheme and (b) without the turbulence scheme. The $0.5\text{ m}^2\text{ s}^{-2}$ isoline (dashed) of turbulence kinetic energy is shown in (a).

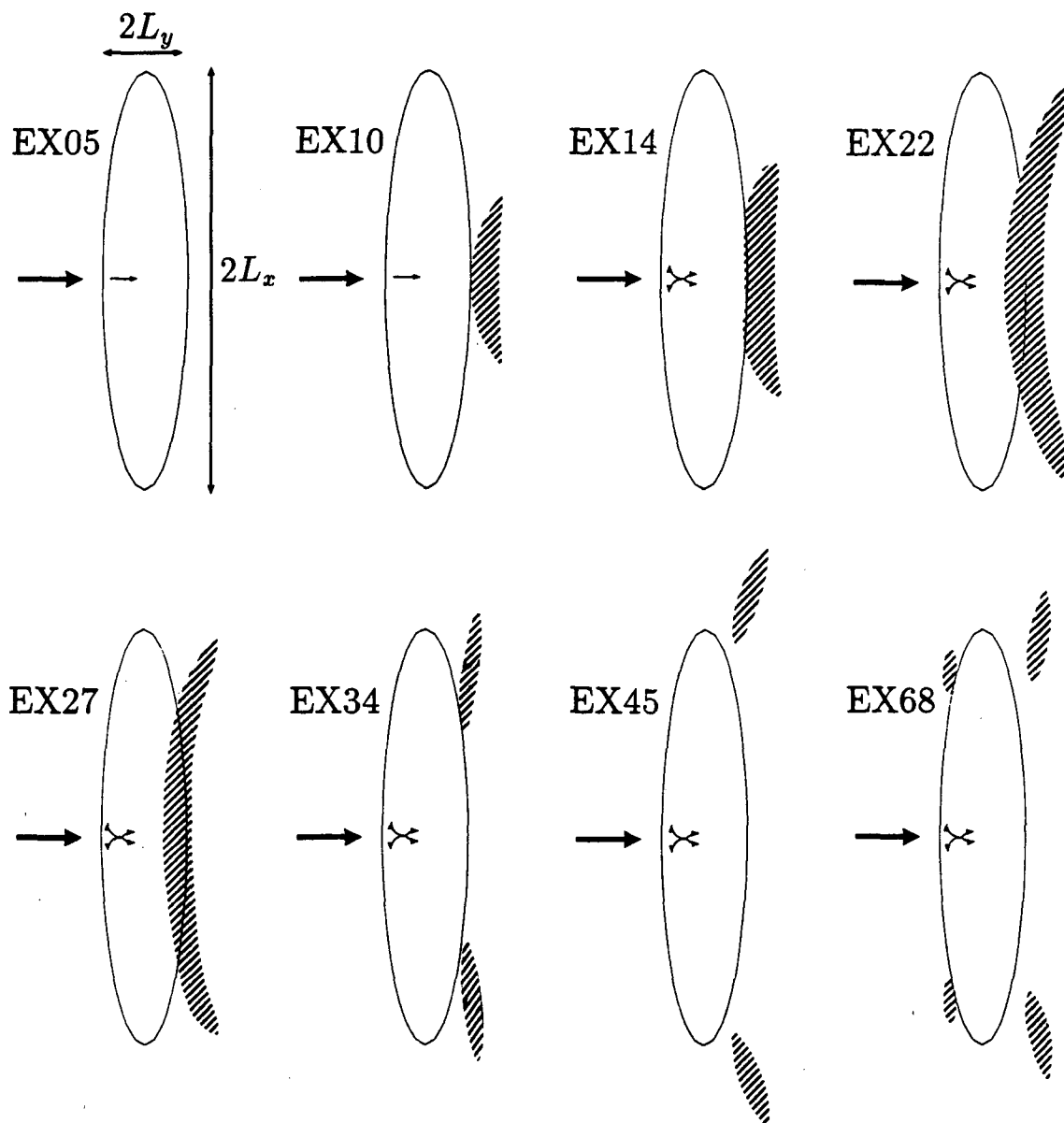


FIG. 14. Horizontal extension of the wave breaking at different values of Nh/U . The bold arrows indicate flow direction, and the thin arrows show flow splitting or no flow splitting.

however, at various regions in the simulations with $Nh/U < 6.818$, and in EX45 the waves are very close to breaking in places corresponding to the wave breaking regions in EX68.

The wave steepening and, in some cases, breaking is closely related to the accelerated flow described in section 6. In fact, the areas of accelerated flow generally form the descending part of a mountain wave. In EX68, the maximum wind speed on the upstream side is reached just before or below the wave breaking zone above the upstream slope (Fig. 16, region **b**). In the other experiments, no wave breaking is related to the

accelerated area upstream of the mountain ridge, although there is considerable steepening in region **b**. The lee-side wave breaking is also located above an area of maximum wind speed (Fig. 16, region **a**).

The wave breaking above the upstream slope in EX68 is closer to the axis of symmetry and at a much higher level than the leeside wave breaking. This is in agreement with the position of the accelerated areas previously described.

Table 1 (line 19) shows the upstream height of the isentrope that acquires maximum steepening 1 cross-stream half-width from the axis of symmetry in the

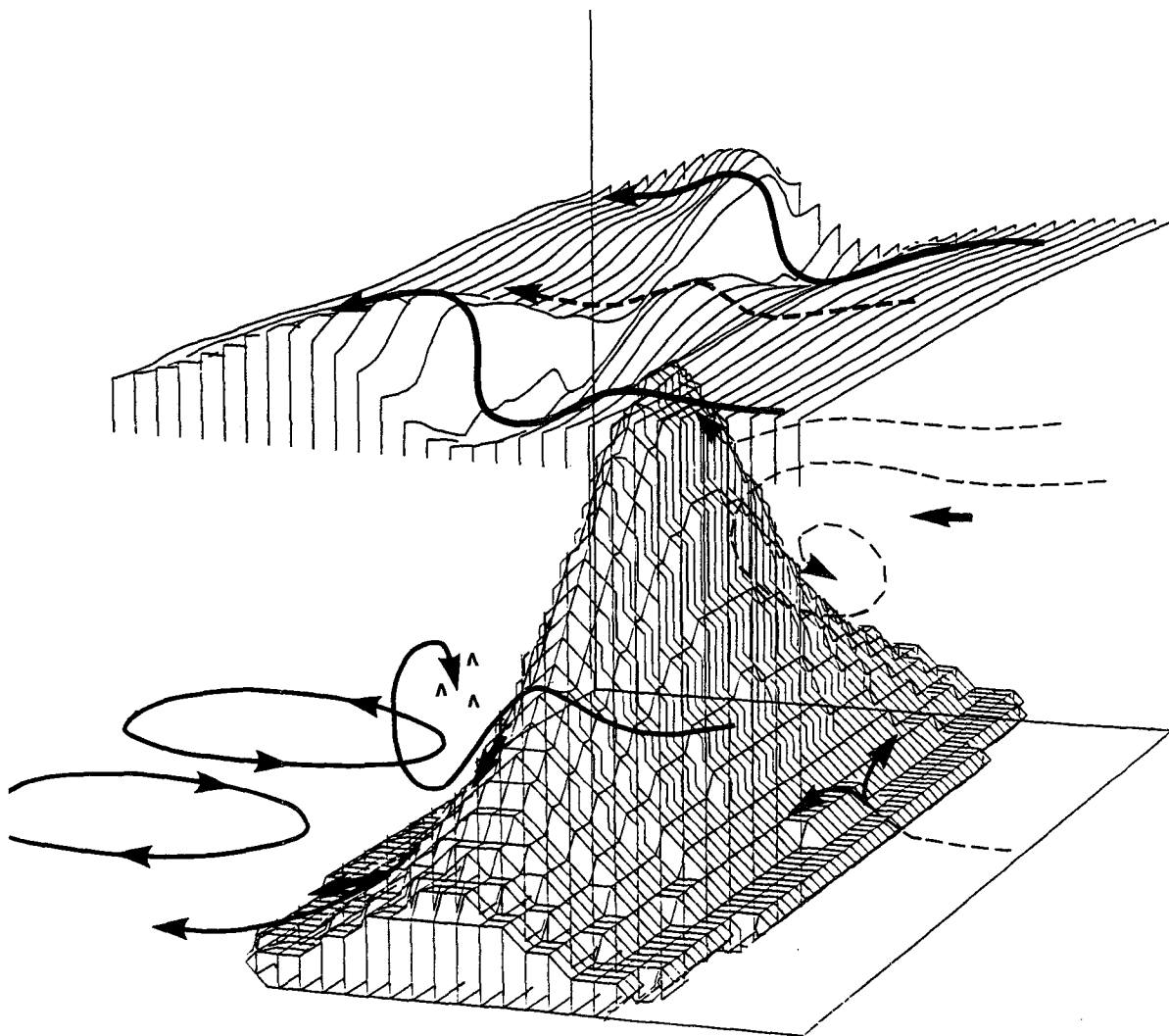


FIG. 15. A schematic perspective of the three-dimensional flow. The bold streamlines are on an isentropic surface, whose upstream height is about $1.1h$ (301 K) in EX45. The dashed streamlines show schematically the flow on the axis of symmetry. Bold arrows that are not connected to a streamline indicate areas of accelerated flow.

different simulations that do not have wave breaking on the axis of symmetry. We see that the levels of maximum steepening and the mountain height are highly correlated. Remembering that the height of the areas of accelerated flow is proportional to the mountain height, this confirms the idea that steepening and wave breaking are related to the accelerated flow. The upper limits of the wave breaking above the lee slope are roughly the same as the upstream height of the isentrope that acquires maximum steepening (Table 1, line 19). We note that this height is about the same as the height of the stagnation point on the windward slope (h_s). This supports the idea that acceleration through deflection plays a major role in creating wave breaking above the lee slope over mountains with high aspect ratio.

The wave breaking in the simulations with high Nh/U is found at a distance of about one cross-stream half-width away from the axis of symmetry. The maximum turbulence is either concentrated in one area or in two areas close together. A study of data from simulations carried out by Stein (1992a) gives similar results; the maximum steepening for a mountain with aspect ratio 5 and $Nh/U = 4.545$ is found to be one cross-stream half-width away from the axis of symmetry.

A simulation with $Nh/U = 4.545$, but $h = 2273$ m, $U = 7.07$ m s⁻¹, and $N = 0.1414$ s⁻¹, gave great steepening but no breaking and no associated concentration of turbulence. This indicates that the wave breaking away from the axis of symmetry may be sensitive to the steepness of the mountain. Another reason could be the nonsimilarity related to the turbulence scheme.

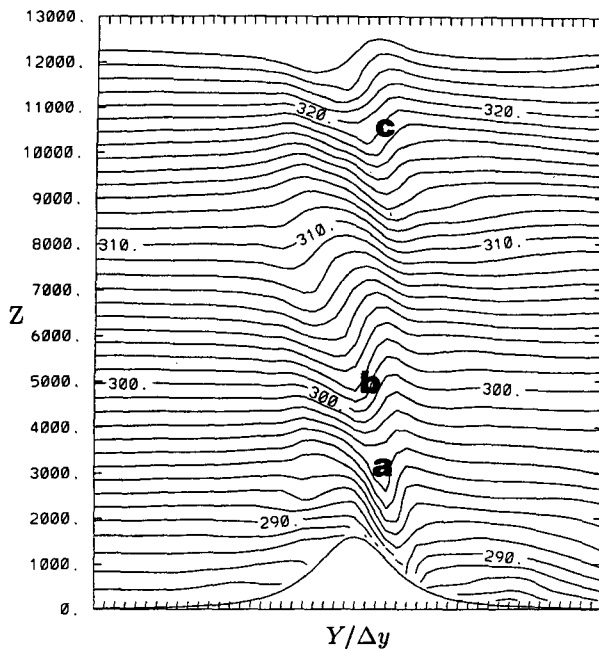


FIG. 16. Isentropes in a cross section 1 cross-stream half-width away from the axis of symmetry in EX45; **a**, **b**, and **c** define regions of wave breaking. For comparison with flow on the axis of symmetry, see Fig. 2.

c. The pressure anomalies and the absence of wave breaking on the axis of symmetry

Why is there no wave breaking on the axis of symmetry in EX34, EX45, and EX68? How may this be explained in view of the results that for all values of Nh/U a substantial part of the flow is diverted vertically rather than horizontally?

On the upstream axis of symmetry there is a fundamental difference between the low-level flow and the upper-level flow, above the stagnation point. The low-level flow forms a blocking, where it is strongly decelerated and partly reversed before being diverted around the mountain. The flow above the stagnation point undergoes less change in speed and is to a much greater extent diverted upward. Meeting the mountain, this part of the flow forms a vertically propagating wave, affected only indirectly by the lower-level flow.

On the basis of this division of the airflow into upper- and lower-level flow, we have attempted to test if Smith's (1989a) linear theory (presented by the diagram in Fig. 3) can be applied locally to predict stagnation aloft in the upper-level flow.

The upstream height of the isentrope arriving at the upper surface stagnation point on the windward slope defines the lower boundary of the upper-level flow. Here N and U are the same as before, but we use a virtual mountain height, $h_u = h - Z_{0s}$, which is the mountain height experienced by the upper-level flow (see Fig. 7). The values of (Nh_u/U) are (in fact) 0.001

times $h - Z_{0s}$ in Table 1. Reading then the regime diagram, we would expect wave breaking in all the experiments. Yet, only simulations with $Nh/U \leq 2.7$ feature wave breaking on the axis of symmetry. The reason for the failure of this method is probably that we have not taken into account the pressure anomaly that is generated by the lower-level flow and its effect on the upper-level flow. However, for the upstream side, we find the pressure anomalies at the upper surface stagnation level to be too similar in all our simulations to be able to explain the absence of wave breaking in EX34, EX45, and EX68. On the upstream side, the pressure anomaly has the form of a well-defined peak, as predicted by linear theory. The lee pressure anomaly has, on the other hand, a greater horizontal extension downstream in the wake. Figure 17 shows the nondimensional surface pressure anomalies on both sides of the mountain together with the drag. On the upstream side, EX05 shows the lowest value of p_{upst}^* . Around the regime transition, p_{upst}^* increases rapidly but slowly for $Nh/U > 1.4$. On the other hand, p_{lee}^* has a maximum in EX10 and decreases for increasing values of Nh/U . The drag and p_{lee}^* show very similar dependence on Nh/U . An equivalent drag dependence on Nh/U for a mountain ridge has been presented by Stein (1992a).

Comparing EX45 and EX45c, we find that the mountain ridge gives about 80% greater pressure drag, about 30% greater p_{upst}^* , and about 90% greater p_{lee}^* than the circular mountain.

The highest absolute value of the lee pressure anomaly in EX14 is connected to the pronounced breaking. As the breaking dies out and a larger part of the flow is deflected horizontally rather than vertically, p_{lee}^* decreases. In EX45, p_{lee}^* is only about one-third of its value in EX10. This decrease in the absolute value of the surface pressure anomaly in the lee of the mountain ridge appears to be connected to increased return flow on the lee side in the simulations with high Nh/U . We have found that by increasing Nh/U , (Nh_u/U) changes very little. In other words we may say that the proportion of horizontally diverted flow increases with increasing Nh/U . The downstream return flow forms a downstream blocking, similar to the upstream blocking. This blocking counteracts descent and wave formation. Table 1 (line 12) shows that the intensity of the return flow depends on Nh/U , which is correlated with the proportion of the horizontally deflected flow. Therefore, it is not surprising that we find a level for Nh/U , above which there is no wave breaking on the axis of symmetry. Finally, we note that the lee-side return flow is strongest on the axis of symmetry, while at a distance of one cross-stream half-width from it there is no return flow. At this point we observe maximum steepening and breaking of the mountain wave.

d. Wave breaking above the upstream slope

Why is there wave breaking above the upstream slope in EX68 but not in the other simulations? In fact,

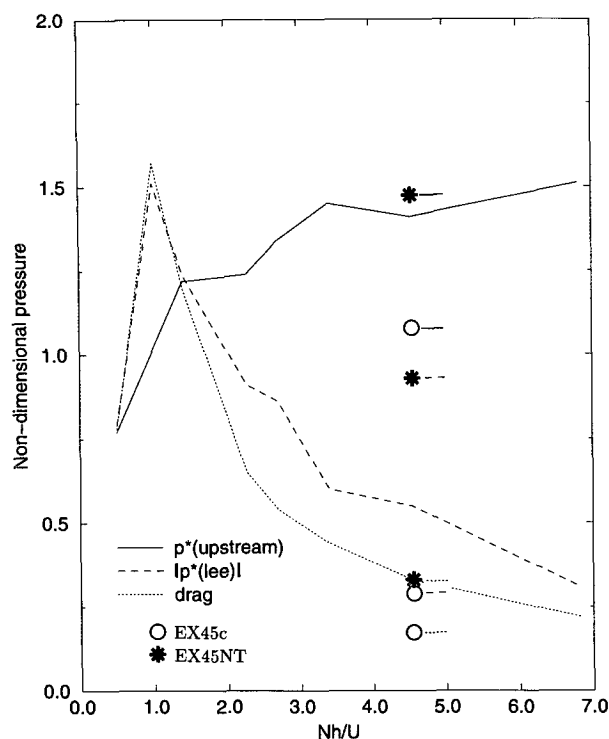


FIG. 17. Maximum values of the normalized pressure anomalies and the drag on the axis of symmetry; $p_{\text{upst/lee}}^* = P_{\text{upst/lee}} / \rho U N h$ and drag $= DL / \rho U N h^2$. The pressure anomaly curves exhibit the mean value of the pressure at two grid points next to each other, featuring the highest pressure anomalies on each side of the mountain. The drag (D) is calculated along a transect $L = 6L_y$; p_{upst}^* is given by a full line, the absolute value of p_{lee}^* by a dashed line, and the drag by a dotted line. Point values from EX45c and EX45NT are also shown.

Smith's (1989b) linear theory predicts the stagnation aloft to occur above the mountaintop, but numerical simulations by Stein (1992a), Smith and Grønås (1993), and others have shown the wave breaking to be above the lee slope. This is in accordance with the wave breaking on the axis of symmetry that we observe in EX10, EX14, EX22, and EX27. The wave breaking above the upstream slope in EX68 is related to the upper areas of accelerated flow, which in turn relate to the upstream blocking. When comparing this to EX22 and EX27, we find that in these cases the upper acceleration starts at a much lower level and much closer to the mountain ridge. The air in the associated gravity wave continues to descend across the mountain crest where the wave breaking takes place. This explains why in EX22 and EX27 wave breaking is found all along the lee slope and not just on the axis of symmetry. At the point of wave breaking in EX22 and EX27 the upper-level accelerated areas have joined the lower-level accelerated areas. In EX45 the upper-level acceleration also starts at a lower level and closer to the mountain ridge than in EX68. The associated wave is very close to breaking above the upstream slope, but

only a very short distance upstream. The fact that the wave breaks in EX68, but not in EX45, is presumably related to slightly stronger wind in EX68 (a difference of $0.07U$).

8. Areas of maximum surface wind

Several papers have related downslope windstorms to mountain wave breaking. This was suggested by Clark and Peltier (1977), and later papers on the issue are discussed by Durran (1990). Table 1 (lines 17 and 18) shows the overall maximum surface wind and the maximum wind observed above the lee slope on the axis of symmetry. The surface wind speed is also shown in Fig. 18. In all cases we find that the overall maximum surface wind is located below a wave breaking zone. However, our simulations show no dramatic increase in wind speeds in relation to the wave breaking. We note, for instance, that the cessation of wave breaking on the axis of symmetry between EX27 and EX34 does not lead to decrease in wind speed. In our experiment with $Nh/U = 4.545$, but with $U = 7.07 \text{ m s}^{-1}$, $N = 0.1414 \text{ s}^{-1}$ and $h = 2273 \text{ m}$, the steepening of the waves away from the axis of symmetry indicates that they are very close to breaking but little turbulence is created. The surface wind is nevertheless only $0.1U$ less than in EX45.

In experiments with values of $Nh/U \leq 1.4$, the maximum surface wind speed is found on the axis of symmetry, but in simulations with higher value of Nh/U , the overall maximum wind speed is found on each side of the axis of symmetry, below the areas of maximum mountain wave steepening. For simulations with increasing values of Nh/U and values greater than 1.4, there is a general tendency for less wind speed on the axis of symmetry and greater wind speed on both sides of it. This corresponds with the fact that as Nh/U increases, wave breaking stops on the axis of symmetry but continues on each side of it. Excluding EX05, which has no wave breaking at all, we find the lowest value of maximum wind speed on the axis of symmetry in EX68. Not unexpectedly, the waves on the axis of symmetry in this simulation are less steep than in the other simulations.

More than one possible reason exists for the absence of a strong downslope windstorm in our simulations. First, the dispersion in our three-dimensional experiments may affect the wave breaking effect (Clark et al. 1994). Second, once the wave breaking has started, our model may simulate the breaking process in such a way that there is little reflection of wave energy. The relatively strong wave activity above the breaking zone indicates that it may be so. This may be resolution dependent. It should also be noted that the typical value of the turbulence kinetic energy ($1\text{--}5 \text{ m}^2 \text{ s}^{-2}$) is far less than what may be related to large-amplitude wave breaking in the vertically structured real atmosphere [e.g., the Boulder windstorm (Richard et al. 1989)].

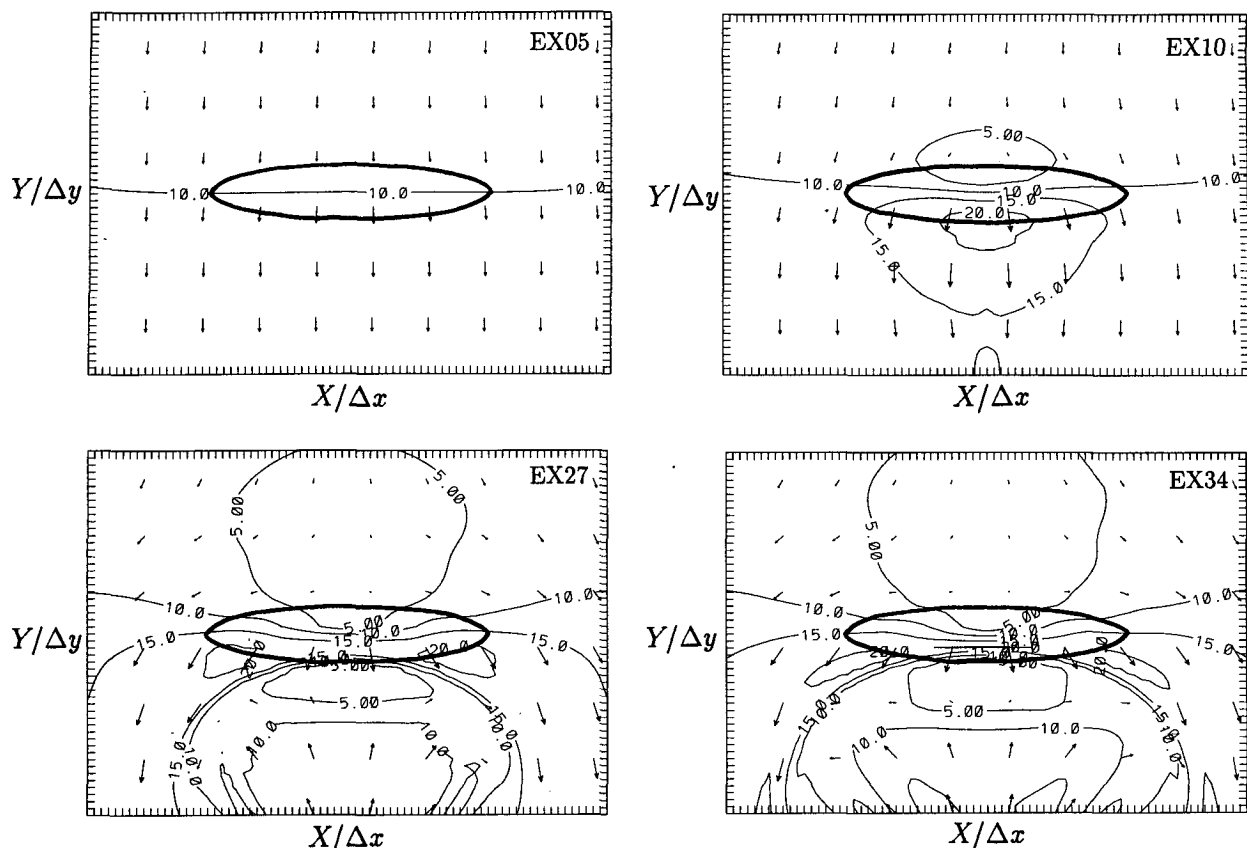


FIG. 18. Surface wind speed in meters per second for different values of Nh/U and $R = 5$. The mountain is shown with an isoline at $0.35h$. The flow is downward.

The region of maximum surface wind propagates arbitrarily downstream from the area of maximum wind speed instead of reaching a stationary state in a limited area. This is coherent with the results of Richard et al. (1989), who studied the role of surface friction in two-dimensional downslope windstorms. They found the region of a downslope windstorm to migrate downwind instead of remaining stationary, as in flow with surface friction.

9. Conclusions

In this paper we have investigated orographic flow past an elliptic mountain. We find Drazin's (1961) theory to be too limited for use in our study of flow with high Nh/U , and we then turned to a numerical approach.

We have found that there is an upper critical value of Nh/U for wave breaking on the axis of symmetry. This value is between 2.7 and 3.4. On each side of the axis of symmetry, wave breaking may, on the other hand, be found for Nh/U as high as 6.818. The study

at hand does not reveal an upper critical value of Nh/U for wave breaking elsewhere than on the axis of symmetry.

Smith's (1989b) linear theory appears to predict well the onset of wave breaking and flow splitting. It is, on the other hand, not useful for predicting an upper critical value of Nh/U for wave breaking. We suggest that by displacing the limit between flow splitting with wave breaking and flow splitting with no wave breaking upward on Smith's (1989b) regime diagram these limits may become meaningful, but as an upper critical value of Nh/U for wave breaking *on the axis of symmetry*.

It appears that this theory cannot be applied locally for high Nh/U to predict wave breaking in the part of the flow that is diverted vertically on the axis of symmetry. A possible reason for this is advection of low-level dense air back toward the mountain by the lee vortices, leading to reduced pressure anomaly.

We observe wave steepening and breaking at various locations on each side of the axis of symmetry. This is apparently a result of a reverse wind shear induced by the three-dimensional flow over and around the moun-

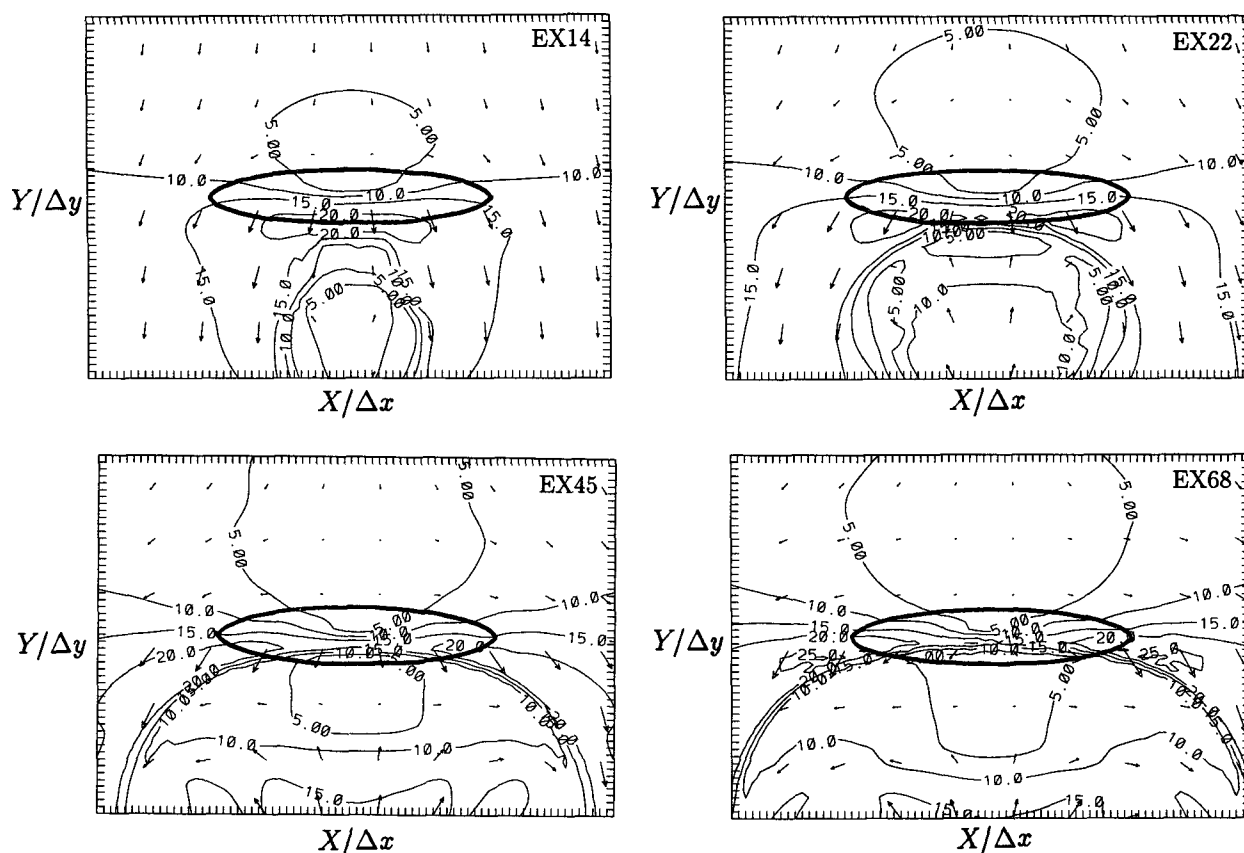


FIG. 18. (Continued)

tain ridge and the upstream blocking. We may call this secondary wave breaking. Studies by Pierrehumbert and Wyman (1985) and Baines and Hoinka (1985) have shown that the onset of flow splitting and the behavior of the blocked flow is highly influenced by the shape of the obstacle. Therefore, we may expect that the secondary wave breaking, which is related to the accelerated areas, is also strongly affected by the shape of the mountain. This effect of mountain shape is more indirect than what is described by Smith (1977) and Lilly and Klemp (1979) and remains to be studied. We note that the values of Nh_b/U , where h_b is the mountain height below the breaking on each side of the axis of symmetry, correspond to values of Nh/U that give wave breaking on Smith's (1989a) regime diagram.

We found that the height of the wave steepening on each side of the axis of symmetry is strongly dependent on the mountain height. This deviates from the two-dimensional theory of Smith (1977), which states that the height of the steepening levels depends only on N and U . This is not surprising, since the wave breaking we describe appears to be a result of a highly three-dimensional nonlinear flow.

We find in our simulations that below breaking waves there is a maximum in the surface wind. However, almost identical surface wind maxima are reached in cases where the above waves are very steep but do not break. In addition, there is in our simulations little decrease in wave amplitude above the layer of turbulent mixing due to breaking. In other words, our hydrostatic model shows far from complete trapping of wave energy below the breaking zones. This does not appear to affect the ability of the turbulence scheme to detect the onset of wave breaking. The absence of strong downslope windstorms in relation to the wave breaking may relate to three-dimensional dispersion or to the coarse horizontal resolution of our numerical model.

At $1.0 < Nh/U < 1.4$, two stagnation points are formed in the upstream surface flow and four in the lee flow. This is connected to major changes in the morphology of the flow. For higher values of Nh/U , more stagnation points tend to form, both on the upstream side and in the lee. These points are, however, not related to significant changes in the flow field.

The height of the upper surface stagnation point (h_s) is proportional to the mountain height (h). This is not

so for the upstream height of the isentrope intersecting the mountain at h_s , (Z_{0s}). By comparing Z_{0s} to h_s , we have found that for a circular mountain the flow on the axis of symmetry may largely split around the mountain without being reversed. This is to a much less extent the case for flow past a mountain with aspect ratio 5.

Significant values of potential vorticity are found at low levels in our free-slip flow. The observed PV pattern is reminiscent of Smith and Schär's (1993) shallow-water vorticity. They related the vorticity generation to dissipation and the joining of two streams of fluid with different values of the Bernoulli function. Our simulation without the turbulence scheme (EX45NT) does not show a decrease but, rather, a slight increase in the PV. We are led to conclude that the dissipation due to the numerical discretization and the horizontal diffusion in our model is more important for PV generation than the dissipation due to the turbulence scheme. The PV increases rapidly with Nh/U close to the onset of flow splitting but slowly for higher values of Nh/U . A further analysis of orographically generated PV in stratified flows will be undertaken and presented in another paper.

Compared to a circular mountain, a mountain ridge with aspect ratio 5 gives twice as much pressure drag, about three times as much turbulence in the upstream blocking, five times faster return flow inside the blocking, about 40% more intense lee vortices, and 30%–60% greater wind speed maxima in the surface flow. Unlike the mountain ridge, the circular mountain produces no secondary wave breaking.

Finally, we have found that ignoring subgrid turbulence does not lead to major changes in the flow. This may, however, not be the case for Nh/U values close to regime transition. In short, the tendency is that no subgrid turbulence gives higher maximum values of wind and somewhat more concentration of potential vorticity.

Acknowledgments. The authors would like to thank Isabelle Beau, Pierre Lacarrère, Valéry Masson, and Joël Stein for helpful discussions and Geneviève Jaubert and Yvan Lemaitre for computer assistance. Haraldur Ólafsson was supported by the Icelandic Council of Science and the Institute for Meteorological Research, Iceland.

REFERENCES

- Baines, P. G., 1987: Upstream blocking and airflow over mountains. *Annu. Rev. Fluid Mech.*, **19**, 75–97.
- , and K. P. Hoinka, 1985: Stratified flow over two-dimensional topography in fluid of infinite depth: A laboratory experiment. *J. Atmos. Sci.*, **42**, 75–97.
- Bougeault, P., and P. Lacarrère, 1989: Parameterization of orography-induced turbulence in a mesobeta-scale model. *Mon. Wea. Rev.*, **117**, 1872–1890.
- , B. Bret, P. Lacarrère, and J. Noilhan, 1991: An experiment with an advanced surface parameterization in a mesobeta-scale model. Part II: The 16 June simulation. *Mon. Wea. Rev.*, **119**, 2374–2392.
- , and Coauthors, 1993: The atmospheric momentum budget over a major mountain range: First results of the PYREX field program. *Ann. Geophys.*, **11**, 395–418.
- Clark, T. J., and W. R. Peltier, 1977: On the evolution and stability of finite-amplitude mountain waves. *J. Atmos. Sci.*, **34**, 1715–1730.
- Clark, T. L., W. D. Hall, and R. M. Banta, 1994: Two- and three-dimensional simulations of the 9 January 1989 severe Boulder windstorm: Comparison with observations. *J. Atmos. Sci.*, **51**, 2317–2343.
- Drazin, P. G., 1961: On the steady flow of a fluid of variable density past an obstacle. *Tellus*, **13**, 239–251.
- Durran, D. R., 1990: Mountain waves and downslope winds. *Atmospheric Processes over Complex Terrain*, Meteor. Monogr., No. 45, Amer. Meteor. Soc., 59–81.
- Eliassen, A., and E. Palm, 1960: On the transfer of energy in stationary mountain waves. *Geophys. Norv.*, **22**, 1–23.
- Förchgott, J., 1949: Vlnové proudění v závětrí horských hřebenu. *Bull. Met. Tchécosl.*, **3**, 49–51.
- Georgelin, M., and E. Richard, 1996: Numerical simulation of flow diversion around the Pyrenees: A tramontana case study. *Mon. Wea. Rev.*, **124**, 687–700.
- , —, M. Petitdidier, and A. Druilhet, 1994: Impact of subgrid-scale orography parameterization on the simulation of orographic flows. *Mon. Wea. Rev.*, **122**, 1509–1522.
- Grubišić, V., R. B. Smith, and C. Schär, 1995: The effect of bottom friction on shallow-water flow past an isolated obstacle. *J. Atmos. Sci.*, **52**, 1985–2005.
- Hunt, C. R., and W. H. Snyder, 1980: Experiments on stably and neutrally stratified flow over a model three-dimensional hill. *J. Fluid Mech.*, **96**, 671–704.
- Hunt, J., C. J. Abell, J. A. Peterka, and H. Woo, 1978: Kinematical studies of the flows around free or surface-mounted obstacles; applying topology to flow visualization. *J. Fluid Mech.*, **95**, 796; Corrigendum, **95**, 796.
- Imbard, M., A. Joly, and R. du Vachat, 1986: Le modèle de prévision numérique PERIDOT: Formulation dynamique et modes de fonctionnement. Tech. Rep. 161, EERM, 70 pp. [Available from CNRM, 42 Av. Coriolis, Toulouse, France.]
- Klemp, J. B., and D. K. Lilly, 1978: Numerical simulation of hydrostatic mountain waves. *J. Atmos. Sci.*, **35**, 78–107.
- Koffi, E. N., 1994: Caractérisation expérimentale de l'écoulement atmosphérique autour d'un massif montagneux (expérience Pyrex). Ph.D. thesis, Université Paul Sabatier, 213 pp.
- Lilly, D. K., and J. B. Klemp, 1979: The effect of terrain shape on nonlinear hydrostatic mountain waves. *J. Fluid Mech.*, **95**, 241–261.
- Masson, V., and P. Bougeault, 1996: Numerical simulations of a low-level wind created by complex orography: A cierzo case study. *Mon. Wea. Rev.*, **124**, 701–715.
- Ólafsson, H., 1996: Atlas des écoulements orographiques et hydrostatiques autour d'un relief idéalisé. Tech. Rep. 42, 86 pp. [Available from CNRM, 42 Av. Coriolis, 31057 Toulouse, France.]
- Phillips, D. S., 1984: Analytical surface pressure and drag for linear hydrostatic flow over three-dimensional elliptical mountains. *J. Atmos. Sci.*, **41**, 1073–1084.
- Pierrehumbert, R. T., and B. Wyman, 1985: Upstream effects of mesoscale mountains. *J. Atmos. Sci.*, **42**, 977–1003.
- Queney, P., 1948: The problem of the airflow over mountains. A summary of theoretical studies. *Bull. Amer. Meteor. Soc.*, **29**, 16–26.
- Richard, E., P. Mascart, and E. C. Nickerson, 1989: The role of surface friction in downslope windstorms. *J. Appl. Meteor.*, **28**, 241–251.
- Satomura, T., and P. Bougeault, 1994: Numerical simulation of lee wave events over the Pyrenees. *J. Meteor. Soc. Japan*, **72**, 173–195.
- Schär, C., and R. Smith, 1993a: Shallow-water flow past isolated topography. Part I: Vorticity production and wave formation. *J. Atmos. Sci.*, **50**, 1373–1400.
- , and —, 1993b: Shallow-water flow past isolated topography. Part II: Transition to vortex shedding. *J. Atmos. Sci.*, **50**, 1401–1412.

- Smith, R. B., 1977: The steepening of hydrostatic mountain waves. *J. Atmos. Sci.*, **34**, 1634–1654.
- , 1980: Linear theory of stratified flow past an isolated mountain. *Tellus*, **32**, 348–364.
- , 1989a: Hydrostatic airflow over mountains. *Advances in Geophysics*, Vol. 31, Academic Press, 59–81.
- , 1989b: Mountain induced stagnation points in hydrostatic flows. *Tellus*, **41A**, 270–274.
- , and S. Grønås, 1993: Stagnation points and bifurcation in 3-D mountain airflow. *Tellus*, **45A**, 28–43.
- Smolarkiewicz, P., and R. Rotunno, 1989: Low Froude number flow past three-dimensional obstacles. Part I: Baroclinically generated lee vortices. *J. Atmos. Sci.*, **46**, 1154–1164.
- , and ———, 1990: Low Froude number flow past three-dimensional obstacles. Part II: Upwind flow reversal zone. *J. Atmos. Sci.*, **47**, 1498–1511.
- Stein, J., 1992a: Contribution à l'étude des régimes hydrostatiques d'écoulements orographiques. Ph.D. thesis, Université Paul Sabatier, 243 pp. [Available from CNRM, 42 Av. Coriolis, Toulouse, France.]
- , 1992b: Investigation of the regime diagram of hydrostatic flow over a mountain with a primitive equations model. Part I: Two-dimensional flows. *Mon. Wea. Rev.*, **120**, 2962–2976.
- Sun, W. Y., and J. D. Chern, 1994: Numerical experiments of vortices in the wakes of large idealized mountains. *J. Atmos. Sci.*, **51**, 191–209.